



The JCMT BISTRO Survey: The Magnetic Fields of the IC 348 Star-forming Region

Youngwoo Choi¹, Woojin Kwon^{2,3,4}, Kate Pattle⁵, Doris Arzoumanian⁶, Tyler L. Bourke^{7,8}, Thiem Hoang^{9,10}, Jihye Hwang⁹, Patrick M. Koch¹¹, Sarah Sadavoy¹², Pierre Bastien¹³, Ray Furuya¹⁴, Shih-Ping Lai^{11,15}, Keping Qiu^{16,17}, Derek Ward-Thompson¹⁸, David Berry¹⁹, Do-Young Byun^{9,10}, Huei-Ru Vivien Chen^{11,15}, Wen Ping Chen²⁰, Mike Chen²¹, Zhiwei Chen²², Tao-Chung Ching²³, Jungyeon Cho²⁴, Minhho Choi⁹, Yunhee Choi⁹, Simon Coudé^{25,26}, Antonio Chrysostomou⁷, Eun Jung Chung⁹, Sophia Dai²⁷, Victor Debattista¹⁸, James Di Francesco^{21,28}, Pham Ngoc Diep²⁹, Yasuo Doi³⁰, Hao-Yuan Duan¹⁵, Yan Duan²⁷, Chakali Eswaraiiah³¹, Lapo Fanciullo³², Jason Fiege³³, Laura M. Fissel¹², Erica Franzmann³³, Per Friberg¹⁹, Rachel Friesen³⁴, Gary Fuller⁸, Tim Gledhill³⁵, Sarah Graves¹⁹, Jane Greaves³⁶, Matt Griffin³⁶, Qilao Gu³⁷, Ilseung Han^{9,10}, Tetsuo Hasegawa³⁸, Martin Houde³⁹, Charles L. H. Hull^{40,41,42}, Tsuyoshi Inoue⁴³, Shu-ichiro Inutsuka⁴⁴, Kazunari Iwasaki⁴⁵, Il-Gyo Jeong^{9,46}, Doug Johnstone^{21,28}, Janik Karoly⁵, Vera Könyves¹⁸, Ji-hyun Kang⁹, Miju Kang⁹, Akimasa Kataoka⁴⁷, Koji Kawabata^{48,49,50}, Francisca Kemper^{51,52,53}, Jongsoo Kim^{9,10}, Shinyoung Kim⁹, Gwanjeong Kim⁵⁴, Kyoung Hee Kim⁹, Mi-Ryang Kim⁵⁵, Kee-Tae Kim^{9,10}, Hyosung Kim², Florian Kirchschlager⁵⁶, Jason Kirk¹⁸, Masato I. N. Kobayashi⁶, Takayoshi Kusune⁵⁷, Jungmi Kwon⁵⁸, Kevin Lacaille^{59,60}, Chi-Yan Law^{61,62}, Chang Won Lee^{9,10}, Hyeseung Lee²⁴, Chin-Fei Lee¹¹, Jeong-Eun Lee^{1,3}, Sang-Sung Lee^{9,10}, Dalei Li⁶³, Di Li⁶⁴, Guangxing Li⁶⁵, Hua-bai Li⁶¹, Sheng-Jun Lin¹⁵, Hong-Li Liu⁶⁵, Tie Liu⁶⁶, Sheng-Yuan Liu¹¹, Junhao Liu¹⁹, Steven Longmore⁶⁷, Xing Lu³⁷, A-Ran Lyo⁹, Steve Mairs¹⁹, Masafumi Matsumura⁶⁸, Brenda Matthews^{21,28}, Gerald Moriarty-Schieven²⁸, Tetsuya Nagata⁶⁹, Fumitaka Nakamura^{47,70}, Hiroyuki Nakanishi⁷¹, Nguyen Bich Ngoc^{29,72}, Nagayoshi Ohashi¹¹, Takashi Onaka⁷³, Geumsook Park⁹, Harriet Parsons¹⁹, Nicolas Peretto³⁶, Felix Priestley³⁶, Tae-Soo Pyo^{70,74}, Lei Qian⁶⁴, Ramprasad Rao¹¹, Jonathan Rawlings⁵, Mark Rawlings^{19,75}, Brendan Retter³⁶, John Richer^{76,77}, Andrew Rigby³⁶, Hiro Saito⁷⁸, Giorgio Savini⁷⁹, Masumichi Seta⁸⁰, Ekta Sharma⁶⁴, Yoshito Shimajiri⁸¹, Hiroko Shinnaga⁷¹, Archana Soam⁸², Mehrnoosh Tahani⁸³, Motohide Tamura^{38,58,84}, Ya-Wen Tang¹¹, Xindi Tang⁸⁵, Kohji Tomisaka⁴⁷, Le Ngoc Tram⁸⁶, Yusuke Tsukamoto⁷¹, Serena Viti⁸⁷, Hongchi Wang²², Jia-Wei Wang^{11,19}, Anthony Whitworth³⁶, Jintai Wu¹⁶, Jinjin Xie²⁷, Meng-Zhe Yang¹⁵, Hsi-Wei Yen¹¹, Hyunju Yoo²⁴, Jinghua Yuan²⁷, Hyeong-Sik Yun⁸⁸, Tetsuya Zenko⁶⁹, Guoyin Zhang⁶⁴, Yapeng Zhang⁸⁹, Chuan-Peng Zhang^{27,64}, Jianjun Zhou⁶³, Lei Zhu⁶⁴, Ilse de Looze⁸⁷, Philippe André⁹⁰, C. Darren Dowell⁹¹, David Eden⁹², Stewart Eyres⁹³, Sam Falle⁹⁴, Valentin J. M. Le Gouellec⁹⁵, Frédéric Poidevin^{96,97}, and Sven van Loo⁹⁸

¹ Department of Physics and Astronomy, Seoul National University, Seoul 08826, Republic of Korea

² Department of Earth Science Education, Seoul National University, 1 Gwanak-ro, Gwanak-gu, Seoul 08826, Republic of Korea; wkwon@snu.ac.kr

³ SNU Astronomy Research Center, Seoul National University, 1 Gwanak-ro, Gwanak-gu, Seoul 08826, Republic of Korea

⁴ The Center for Educational Research, Seoul National University, 1 Gwanak-ro, Gwanak-gu, Seoul 08826, Republic of Korea

⁵ Department of Physics and Astronomy, University College London, Gower Street, London WC1E 6BT, UK

⁶ Division of Science, National Astronomical Observatory of Japan, 2-21-1 Osawa, Mitaka, Tokyo 181-8588, Japan

⁷ SKA Observatory, Jodrell Bank, Lower Withington, Macclesfield SK11 9FT, UK

⁸ Jodrell Bank Centre for Astrophysics, School of Physics and Astronomy, University of Manchester, Oxford Road, Manchester, UK

⁹ Korea Astronomy and Space Science Institute, 776 Daedeok-daero, Yuseong-gu, Daejeon 34055, Republic of Korea

¹⁰ University of Science and Technology, Korea, 217 Gajeong-ro, Yuseong-gu, Daejeon 34113, Republic of Korea

¹¹ Academia Sinica Institute of Astronomy and Astrophysics, No. 1, Sec. 4., Roosevelt Road, Taipei 106216, Taiwan

¹² Department for Physics, Engineering Physics and Astrophysics, Queen's University, Kingston, ON K7L 3N6, Canada

¹³ Centre de recherche en astrophysique du Québec & département de physique, Université de Montréal, 1375 Avenue Thérèse-Lavoie-Roux, Montréal, QC H2V 0B3, Canada

¹⁴ Institute of Liberal Arts and Sciences Tokushima University, Minami Jousanajima-machi 1-1, Tokushima 770-8502, Japan

¹⁵ Institute of Astronomy and Department of Physics, National Tsing Hua University, Hsinchu 30013, Taiwan

¹⁶ School of Astronomy and Space Science, Nanjing University, 163 Xianlin Avenue, Nanjing 210023, People's Republic of China

¹⁷ Key Laboratory of Modern Astronomy and Astrophysics (Nanjing University), Ministry of Education, Nanjing 210023, People's Republic of China

¹⁸ Jeremiah Horrocks Institute, University of Central Lancashire, Preston PR1 2HE, UK

¹⁹ East Asian Observatory, 660 N. A'ohōkū Place, University Park, Hilo, HI 96720, USA

²⁰ Institute of Astronomy, National Central University, Zhongli 32001, Taiwan

²¹ Department of Physics and Astronomy, University of Victoria, Victoria, BC V8W 2Y2, Canada

²² Purple Mountain Observatory, Chinese Academy of Sciences, 2 West Beijing Road, 210008 Nanjing, People's Republic of China

²³ National Radio Astronomy Observatory, 1003 Lopezville Road, Socorro, NM 87801, USA

²⁴ Department of Astronomy and Space Science, Chungnam National University, Daejeon 34134, Republic of Korea

²⁵ Department of Earth, Environment, and Physics, Worcester State University, Worcester, MA 01602, USA

²⁶ Center for Astrophysics | Harvard & Smithsonian, 60 Garden Street, Cambridge, MA 02138, USA

²⁷ National Astronomical Observatories, Chinese Academy of Sciences, A20 Datun Road, Chaoyang District, Beijing 100012, People's Republic of China

²⁸ NRC Herzberg Astronomy and Astrophysics, 5071 West Saanich Road, Victoria, BC V9E 2E7, Canada

²⁹ Vietnam National Space Center, Vietnam Academy of Science and Technology, Hanoi, Vietnam

³⁰ Department of Earth Science and Astronomy, Graduate School of Arts and Sciences, The University of Tokyo, 3-8-1 Komaba, Meguro, Tokyo 153-8902, Japan

³¹ Department of Physics, Indian Institute of Science Education and Research (IISER) Tirupati, Yerpedu, Tirupati - 517619, Andhra Pradesh, India

³² National Chung Hsing University, 145 Xingda Road, South Dist., Taichung City 402, Taiwan

³³ Department of Physics and Astronomy, The University of Manitoba, Winnipeg, Manitoba R3T2N2, Canada

³⁴ National Radio Astronomy Observatory, 520 Edgemont Road, Charlottesville, VA 22903, USA

³⁵ School of Physics, Astronomy & Mathematics, University of Hertfordshire, College Lane, Hatfield, Hertfordshire AL10 9AB, UK

³⁶ School of Physics and Astronomy, Cardiff University, The Parade, Cardiff, CF24 3AA, UK

³⁷ Shanghai Astronomical Observatory, Chinese Academy of Sciences, 80 Nandan Road, Shanghai 200030, People's Republic of China

- ³⁸ National Astronomical Observatory of Japan, National Institutes of Natural Sciences, Osawa, Mitaka, Tokyo 181-8588, Japan
- ³⁹ Department of Physics and Astronomy, The University of Western Ontario, 1151 Richmond Street, London N6A 3K7, Canada
- ⁴⁰ National Astronomical Observatory of Japan, Alonso de Córdova 3788, Office 61B, Vitacura, Santiago, Chile
- ⁴¹ Joint ALMA Observatory, Alonso de Córdova 3107, Vitacura, Santiago, Chile
- ⁴² NAOJ Fellow
- ⁴³ Department of Physics, Konan University, Okamoto 8-9-1, Higashinada-ku, Kobe 658-8501, Japan
- ⁴⁴ Department of Physics, Graduate School of Science, Nagoya University, Furo-cho, Chikusa-ku, Nagoya 464-8602, Japan
- ⁴⁵ Department of Environmental Systems Science, Doshisha University, Tatakae, Miyakodani 1-3, Kyotanabe, Kyoto 610-0394, Japan
- ⁴⁶ Department of Astronomy and Atmospheric Sciences, Kyungpook National University, Republic of Korea
- ⁴⁷ Division of Theoretical Astronomy, National Astronomical Observatory of Japan, Mitaka, Tokyo 181-8588, Japan
- ⁴⁸ Hiroshima Astrophysical Science Center, Hiroshima University, Kagamiyama 1-3-1, Higashi-Hiroshima, Hiroshima 739-8526, Japan
- ⁴⁹ Department of Physics, Hiroshima University, Kagamiyama 1-3-1, Higashi-Hiroshima, Hiroshima 739-8526, Japan
- ⁵⁰ Core Research for Energetic Universe, Hiroshima University, Kagamiyama 1-3-1, Higashi-Hiroshima, Hiroshima 739-8526, Japan
- ⁵¹ Institute of Space Sciences (ICE), CSIC, Can Magrans, 08193 Cerdanyola del Vallés, Barcelona, Spain
- ⁵² ICREA, Pg. Lluís Companys 23, Barcelona, Spain
- ⁵³ Institut d'Estudis Espacials de Catalunya (IEEC), E-08034 Barcelona, Spain
- ⁵⁴ Nobeyama Radio Observatory, National Astronomical Observatory of Japan, National Institutes of Natural Sciences, Nobeyama, Minamimaki, Minamisaku, Nagano 384-1305, Japan
- ⁵⁵ School of Space Research, Kyung Hee University, 1732 Deogyong-daero, Giheung-gu, Yongin-si, Gyeonggi-do 17104, Republic of Korea
- ⁵⁶ Sterrenkundig Observatorium, Ghent University, Krijgslaan 281-S9, 9000 Gent, Belgium
- ⁵⁷ Astronomical Institute, Graduate School of Science, Tohoku University, Aoba-ku, Sendai, Miyagi 980-8578, Japan
- ⁵⁸ Department of Astronomy, Graduate School of Science, University of Tokyo, 7-3-1 Hongo, Bunkyo-ku, Tokyo 113-0033, Japan
- ⁵⁹ Department of Physics and Astronomy, McMaster University, Hamilton, ON L8S 4M1, Canada
- ⁶⁰ Department of Physics and Atmospheric Science, Dalhousie University, Halifax, NS B3H 4R2, Canada
- ⁶¹ Department of Physics, The Chinese University of Hong Kong, Shatin, N.T., Hong Kong
- ⁶² Department of Space, Earth & Environment, Chalmers University of Technology, SE-412 96 Gothenburg, Sweden
- ⁶³ Xinjiang Astronomical Observatory, Chinese Academy of Sciences, Urumqi 830011, Xinjiang, People's Republic of China
- ⁶⁴ CAS Key Laboratory of FAST, National Astronomical Observatories, Chinese Academy of Sciences, People's Republic of China
- ⁶⁵ Department of Astronomy, Yunnan University, Kunming, 650091, People's Republic of China
- ⁶⁶ Key Laboratory for Research in Galaxies and Cosmology, Shanghai Astronomical Observatory, Chinese Academy of Sciences, 80 Nandan Road, Shanghai 200030, People's Republic of China
- ⁶⁷ Astrophysics Research Institute, Liverpool John Moores University, 146 Brownlow Hill, Liverpool L3 5RF, UK
- ⁶⁸ Faculty of Education & Center for Educational Development and Support, Kagawa University, Saiwai-cho 1-1, Takamatsu, Kagawa, 760-8522, Japan
- ⁶⁹ Department of Astronomy, Graduate School of Science, Kyoto University, Sakyo-ku, Kyoto 606-8502, Japan
- ⁷⁰ SOKENDAI (The Graduate University for Advanced Studies), Hayama, Kanagawa 240-0193, Japan
- ⁷¹ Department of Physics and Astronomy, Graduate School of Science and Engineering, Kagoshima University, 1-21-35 Korimoto, Kagoshima 890-0065, Japan
- ⁷² Graduate University of Science and Technology, Vietnam Academy of Science and Technology, Hanoi, Vietnam
- ⁷³ Department of Astronomy, Graduate School of Science, The University of Tokyo, 7-3-1 Hongo, Bunkyo-ku, Tokyo 113-0033, Japan
- ⁷⁴ Subaru Telescope, National Astronomical Observatory of Japan, 650 N. A'ohōkū Place, Hilo, HI 96720, USA
- ⁷⁵ Gemini Observatory/NSF NOIRLab, 670 N. A'ohōkū Place, Hilo, HI 96720, USA
- ⁷⁶ Astrophysics Group, Cavendish Laboratory, J. J. Thomson Avenue, Cambridge CB3 0HE, UK
- ⁷⁷ Kavli Institute for Cosmology, Institute of Astronomy, University of Cambridge, Madingley Road, Cambridge, CB3 0HA, UK
- ⁷⁸ Faculty of Pure and Applied Sciences, University of Tsukuba, 1-1-1 Tennodai, Tsukuba, Ibaraki 305-8577, Japan
- ⁷⁹ OSL, Physics & Astronomy Dept., University College London, WC1E 6BT London, UK
- ⁸⁰ Department of Physics, School of Science and Technology, Kwansai Gakuin University, 2-1 Gakuen, Sanda, Hyogo 669-1337, Japan
- ⁸¹ Kyushu Kyoritsu University, 1-8, Jiyugaoka, Yahatanishi-ku, Kitakyushu-shi, Fukuoka 807-8585, Japan
- ⁸² Indian Institute of Astrophysics, II Block, Koramangala, Bengaluru 560034, India
- ⁸³ Banting and KIPAC Fellowships: Kavli Institute for Particle Astrophysics & Cosmology (KIPAC), Stanford University, Stanford, CA 94305, USA
- ⁸⁴ Astrobiology Center, National Institutes of Natural Sciences, 2-21-1 Osawa, Mitaka, Tokyo 181-8588, Japan
- ⁸⁵ Xinjiang Astronomical Observatory, Chinese Academy of Sciences, 830011 Urumqi, People's Republic of China
- ⁸⁶ Leiden Observatory, Leiden University, PO Box 9513, 2300 RA Leiden, The Netherlands
- ⁸⁷ Physics & Astronomy Dept., University College London, WC1E 6BT London, UK
- ⁸⁸ Korea Astronomy and Space Science Institute, Yuseong-gu, Daejeon 34055, Republic of Korea
- ⁸⁹ Department of Astronomy, Beijing Normal University, Beijing 100875, People's Republic of China
- ⁹⁰ Laboratoire d'Astrophysique (AIM), Université Paris-Saclay, Université Paris Cité, CEA, CNRS, AIM, 91191 Gif-sur-Yvette, France
- ⁹¹ Jet Propulsion Laboratory, M/S 169-506, 4800 Oak Grove Drive, Pasadena, CA 91109, USA
- ⁹² Armagh Observatory and Planetarium, College Hill, Armagh BT61 9DB, UK
- ⁹³ University of South Wales, Pontypridd, CF37 1DL, UK
- ⁹⁴ Department of Applied Mathematics, University of Leeds, Woodhouse Lane, Leeds LS2 9JT, UK
- ⁹⁵ NASA Ames Research Center, Space Science and Astrobiology Division M.S. 245-6, Moffett Field, CA 94035, USA
- ⁹⁶ Instituto de Astrofísica de Canarias, 38200 La Laguna, Tenerife, Canary Islands, Spain
- ⁹⁷ Departamento de Astrofísica, Universidad de La Laguna (ULL), 38206 La Laguna, Tenerife, Spain
- ⁹⁸ School of Physics and Astronomy, University of Leeds, Woodhouse Lane, Leeds LS2 9JT, UK

Received 2024 June 18; revised 2024 October 15; accepted 2024 October 17; published 2024 November 29

Abstract

We present 850 μm polarization observations of the IC 348 star-forming region in the Perseus molecular cloud as part of the B-fields In STar-forming Region Observation survey. We study the magnetic properties of two cores (HH 211 MMS and IC 348 MMS) and a filamentary structure of IC 348. We find that the overall field tends to be

more perpendicular than parallel to the filamentary structure of the region. The polarization fraction decreases with intensity, and we estimate the trend by power law and the mean of the Rice distribution fittings. The power indices for the cores are much smaller than 1, indicative of possible grain growth to micron size in the cores. We also measure the magnetic field strengths of the two cores and the filamentary area separately by applying the Davis–Chandrasekhar–Fermi method and its alternative version for compressed medium. The estimated mass-to-flux ratios are 0.45–2.20 and 0.63–2.76 for HH 211 MMS and IC 348 MMS, respectively, while the ratios for the filament are 0.33–1.50. This result may suggest that the transition from subcritical to supercritical conditions occurs at the core scale (~ 0.05 pc) in the region. In addition, we study the energy balance of the cores and find that the relative strength of turbulence to the magnetic field tends to be stronger for IC 348 MMS than for HH 211 MMS. The result could potentially explain the different configurations inside the two cores: a single protostellar system in HH 211 MMS and multiple protostars in IC 348 MMS.

Unified Astronomy Thesaurus concepts: [Interstellar medium \(847\)](#); [Interstellar magnetic fields \(845\)](#); [Interstellar filaments \(842\)](#); [Molecular clouds \(1072\)](#); [Star formation \(1569\)](#); [Polarimetry \(1278\)](#); [Submillimeter astronomy \(1647\)](#)

1. Introduction

Molecular clouds are the densest and coldest regions of the interstellar medium (ISM), where new stars are born. Recent observations toward nearby molecular clouds made by Herschel revealed that molecular clouds have highly filamentary structures (e.g., P. André et al. 2010; D. Arzoumanian et al. 2011; P. Palmeirim et al. 2013). Molecular cores lie along filaments, forming new stars by gravitational collapse (e.g., A. Hacar et al. 2013; M. Fernández-López et al. 2014; K. Pattle et al. 2023).

One of the crucial recent findings is that these filamentary structures are strongly affected by local magnetic fields (e.g., P. Palmeirim et al. 2013; N. L. J. Cox et al. 2016; Planck Collaboration et al. 2016; D. Ward-Thompson et al. 2017; K. Pattle et al. 2023). The magnetic fields are perpendicular to high column density filaments, while they are parallel to lower dense subfilaments or striations (e.g., N. L. J. Cox et al. 2016; T. Liu et al. 2018; D. Alina et al. 2019; L. M. Fissel et al. 2019; A. Soam et al. 2019; Y. Doi et al. 2020; T. G. S. Pillai et al. 2020; D. Arzoumanian et al. 2021; T.-C. Ching et al. 2022b; W. Kwon et al. 2022; D. Ward-Thompson et al. 2023). The observed field morphology can be explained by the magnetic funneling scenario, in which diffuse matter moves through subfilaments along the field lines, feeding materials to the main filaments (J. D. Soler et al. 2013; P. André et al. 2014; K. Pattle et al. 2023).

Other prominent features of molecular clouds are that they are significantly hierarchical (R. Pokhrel et al. 2018) and have a lifetime longer than the freefall timescale. Large clouds fragment into small clumps or filamentary systems and form smaller cores inside a filament. This whole process is known to be far slower than the freefall collapse of clouds, given that star formation efficiency in nearby molecular clouds is estimated to be less than 5% (e.g., J. M. Carpenter 2000; N. J. I. Evans et al. 2009; A. T. Barnes et al. 2017). This indicates that the star formation process is not only regulated by gravity and thermal pressure but also affected by other processes like magnetic fields and turbulence (e.g., P. Padoan et al. 2014). The relative importance of these four properties determines star formation efficiency and how molecular clouds fragment into smaller structures (Y.-W. Tang et al. 2019; E. J. Chung et al. 2023). Therefore, estimating the relative strengths between the energy densities of gravity, thermal pressure, turbulence, and magnetic fields on different scales in molecular clouds is vital to understanding the star formation process (e.g., K. Pattle et al. 2017a; S. Coudé et al. 2019; J. Liu et al. 2019; J.-W. Wang

et al. 2019; J. Hwang et al. 2021, 2022; A. R. Lyo et al. 2021; E. J. Chung et al. 2023; M. Tahani et al. 2023).

Magnetic properties of molecular clouds can be studied through dust polarization observations. Nonspherical grains can be spun up to suprathermal by radiative torques and become aligned with their shortest axis parallel to the ambient magnetic fields (B. T. Draine & J. C. Weingartner 1997; A. Lazarian & T. Hoang 2007). This grain alignment process includes the alignment of the grain shortest axis with its angular momentum (internal alignment) caused by internal relaxation processes (E. M. Purcell 1979) and the alignment of the grain angular momentum with the magnetic field (external alignment) caused by radiative torques and magnetic relaxation (e.g., T. Hoang & A. Lazarian 2016). As a result, continuum emission from dust grains is linearly polarized along the direction of the grain longer axis, which is perpendicular to the magnetic field. This allows us to infer the magnetic field orientations projected on the plane of the sky by rotating 90° the linear polarization angles observed at far-IR to (sub) millimeter wavelengths (e.g., B. C. Matthews et al. 2009). Note that, in contrast, the background radiation at optical and near-infrared wavelengths is extinguished by aligned dust grains, resulting in polarization parallel to the magnetic field directions (L. J. Davis & J. L. Greenstein 1951).

The Perseus giant molecular cloud complex is one of the largest and nearest sites in which numerous young stars are born. It contains various star-forming molecular clouds, including IC 348, NGC 1333, B1, L1448, and L1455 (H. Kirk et al. 2007). Hundreds of young stars are born in the Perseus giant molecular cloud (J. Bally et al. 2008), and most belong to two clusters, IC 348 and NGC 1333 (W. Herbst 2008; J. Walawender et al. 2008; K. L. Luhman et al. 2016). IC 348 is located in the eastern part of the Perseus molecular cloud complex. The distance of IC 348 is estimated to be around 321 pc from trigonometric parallax observations (G. N. Ortiz-León et al. 2018) and 295 pc from a combination of stellar photometry, parallax measurement, and CO observations (C. Zucker et al. 2018). We assumed a distance of 300 pc, with an uncertainty of 10%. IC 348 contains a large number of pre-main-sequence stars and protostars (W. Herbst 2008), and the age of IC 348 is from 2 to 6 Myr based on evolutionary models (K. L. Luhman et al. 2003; C. P. M. Bell et al. 2013). Most pre-main-sequence stars are concentrated within the central region, whereas protostars lie in the southwestern ridge part (W. Herbst 2008). In this paper, we focus on the southwestern part of IC 348, also known as IC 348-SW. Two

cores (HH 211 MMS and IC 348 MMS) host Class 0 protostars in IC 348-SW (J. Eisloffel et al. 2003), and we study the magnetic properties of the filamentary structure and the two cores.

This study was conducted as part of the B-Fields in Star-forming Region Observations (BISTRO) survey (D. Ward-Thompson et al. 2017), one of the James Clerk Maxwell Telescope (JCMT) large programs. The BISTRO survey observes molecular clouds of the Gould Belt (J. F. W. S. Herschel 1847; B. A. Gould 1879) to investigate the role of magnetic fields in star formation (D. Ward-Thompson et al. 2017) and has been extended to BISTRO-2 and BISTRO-3 for further and/or massive star-forming regions. IC 348 is a target of BISTRO-2.

In this paper, we present 850 μm polarization observations toward the IC 348 star-forming region. Observations and data reduction are described in Section 2. In Section 3, we show the magnetic field morphology of IC 348. We also discuss the dependence of the polarization fraction on total intensity by power law and the mean of the Rice distribution fittings in Section 4. In Section 5, we estimate the magnetic field strengths of the two cores and the filament. In Section 6, we study the energy balances of the two core regions. We discuss the aligned grain size, magnetic criticality, and stability of the target region in Section 7. Finally, we summarize our conclusions in Section 8.

2. Observations

JCMT is a 15 m single-dish radio telescope located at an altitude of 4092 m in Maunakea, Hawaii. The Submillimeter Common User Bolometer Array-2 (SCUBA-2) mounted on JCMT has a 10,000-pixel submillimeter continuum and simultaneously observes in the 450 μm and 850 μm atmospheric windows (W. S. Holland et al. 2013). Furthermore, to obtain polarization data, the POL-2 polarimeter is installed in the pathway of the SCUBA-2 camera and observes the sky in a daisy-like pattern at a speed of 8'' s⁻¹ (P. Friberg et al. 2016).

We observed the IC 348 star-forming region with POL-2 between 2019 October and 2020 February as part of the BISTRO survey (Project ID: M17BL011). Observations of 20 repetitions were made for 40 minutes each, to reach a total of about 14 hr under Band 1 weather conditions ($\tau_{225 \text{ GHz}} < 0.05$), using the POL-2 DAISY scan mode (P. Friberg et al. 2016). In addition to BISTRO observations, 16 sets of polarization data (30 minutes each) were taken between 2017 July (Project ID: M17AP073) and September (Project ID: M17BP058) under Band 2 weather conditions ($0.05 < \tau_{225 \text{ GHz}} < 0.08$; PI: Woojin Kwon). These additional data were combined with BISTRO observations. The rms noises of the final Stokes I and Stokes Q and U maps at 850 μm are 3.3 and 2.5 mJy beam⁻¹, respectively.

The observational data were reduced using the *pol2map* command of the SMURF package of STARLINK (M. J. Currie et al. 2014). This reduction process comprises three steps. First, the *calcqu* command creates Stokes I , Q , and U time streams from the raw bolometer time streams for each observation. Then, the initial Stokes I map is created by coadding I time streams using the iterative mapmaking routine *makemap* (E. L. Chapin et al. 2013). In the next stage, the pointing corrections and signal-to-noise ratio (S/N)-based fixed mask determined from the initial I map are applied to reproduce a Stokes I map. In this step, instead of the *makemap* routine, the

skyloop command is used to generate a combined map from all the observations. In the last step, the Stokes Q and U maps are produced using the output masks created in the second stage. The final Stokes I map is used for instrumental polarization (IP) correction of the final Q and U maps. We use the ‘‘2019 August’’ IP model⁹⁹ for IP correction. The pixel size of the final I , Q , and U maps is set to 4''. Lastly, the final half-vector catalog of polarizations is made from the final I , Q , and U maps on a bin size of 12'', similar to the beam size of SCUBA-2 at 850 μm , 14''6.

In this study, we use the 850 μm I , Q , and U maps to infer the magnetic properties of the IC 348 star-forming region. The I map at 450 μm is also used to calculate the dust temperature and column density distributions of the target with the 850 μm I map. The effective FWHMs of the SCUBA-2 beams are 14.''6 and 9.''8 at 850 μm and 450 μm , respectively (J. T. Dempsey et al. 2013). The flux conversion factors (FCFs) of SCUBA-2 at 850 μm are 495 Jy pW⁻¹ beam⁻¹ after 2018 June and 516 Jy pW⁻¹ beam⁻¹ from 2016 November to 2018 June. At 450 μm , the values are 472 Jy pW⁻¹ beam⁻¹ after 2018 June and 531 Jy pW⁻¹ beam⁻¹ before 2018 June (S. Mairs et al. 2021). Weighted by the observational time, we adopt 503 Jy pW⁻¹ beam⁻¹ at 850 μm and 495 Jy pW⁻¹ beam⁻¹ at 450 μm for FCF values of SCUBA-2. These values were multiplied by transmission corrector factors for POL-2, which are 1.35 and 1.96 at 850 μm and 450 μm , respectively (P. Friberg et al. 2016). Therefore, in this paper we apply the FCF values of 679 Jy pW⁻¹ beam⁻¹ at 850 μm and 970 Jy pW⁻¹ beam⁻¹ at 450 μm .

We also use the C¹⁸O $J = 3 \rightarrow 2$ data at the rest frequency of 329.278 GHz to infer turbulent motions of the target region, which were taken under the project code M06BGT02 and first published by E. I. Curtis et al. (2010) using the reduction performed by the JCMT Gould Belt Survey (D. Ward-Thompson et al. 2007). The survey observed nearby low-mass and intermediate-mass star-forming regions, including IC 348, with SCUBA-2 and the Heterodyne Array Receiver Program (HARP). HARP offers large-scale velocity maps of a high spectral resolution with 16 heterodyne pixels (J. V. Buckle et al. 2009). The pixel size and spectral resolution of the map are 7'' and 0.1 km s⁻¹, respectively. The rms noise of the spectra is 0.22 K.

3. Magnetic Field Morphology

Figure 1 shows two core regions and a filamentary structure of the IC 348 star-forming region. We define the area where 850 μm intensities are greater than 0.3 Jy beam⁻¹ (90 σ) and 0.05 Jy beam⁻¹ (15 σ) as the core region and filament region, respectively.

Polarization properties are inferred from the Stokes I , Q , and U maps obtained from the data reduction process described in the previous section. In principle, from the Q and U map values, polarized intensity (PI) is calculated as

$$\text{PI}_{\text{non-debiased}} = \sqrt{Q^2 + U^2}, \quad (1)$$

where Q and U represent Stokes Q and U values, respectively. However, since the PI is defined as a sum of squared Stokes Q and U values, errors of the Stokes Q and U lead to an overestimation in the measured PI. This positive bias is usually

⁹⁹ <https://www.eaoobservatory.org/jcmt/2019/08/new-ip-models-for-pol2-data/>

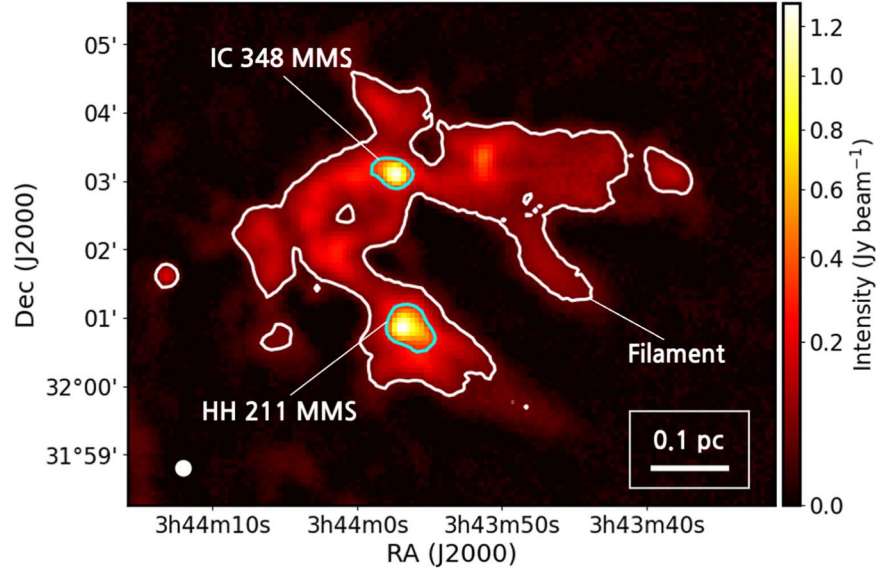


Figure 1. Positions of HH 211 MMS and IC 348 MMS (or IC 348 SMM2) in the IC 348 star-forming region at the total intensity map of 850 μm . Cyan and white contours are at total intensities of 0.3 and 0.05 Jy beam^{-1} , respectively, representing the core and filament regions. The beam and the spatial scale bar are shown in the lower left and right corners, respectively.

corrected using the uncertainty in the Q and U values:

$$\text{PI}_{\text{debiased}} = \sqrt{Q^2 + U^2 - 0.5(\delta Q^2 + \delta U^2)}, \quad (2)$$

where δQ and δU represent uncertainties in the Stokes Q and U , respectively (J. F. C. Wardle & P. P. Kronberg 1974). The uncertainty of PI is given by

$$\delta \text{PI} = \sqrt{\frac{Q^2 \delta Q^2 + U^2 \delta U^2}{Q^2 + U^2}}. \quad (3)$$

The polarization fraction and its uncertainty are

$$P = \frac{\text{PI}}{I} \quad (4)$$

and

$$\delta P = \sqrt{\frac{\delta \text{PI}^2}{I^2} + \frac{\delta I^2 (Q^2 + U^2)}{I^4}}, \quad (5)$$

where I and δI represent a Stokes I value and its uncertainty, respectively.

Lastly, the polarization angle and its uncertainty are calculated as follows:

$$\theta_p = \frac{1}{2} \arctan\left(\frac{U}{Q}\right) \quad (6)$$

and

$$\delta \theta_p = \frac{1}{2} \sqrt{\frac{Q^2 \delta U^2 + U^2 \delta Q^2}{Q^2 + U^2}}. \quad (7)$$

The left panel of Figure 2 shows 850 μm polarization angles within the IC 348 star-forming region. Polarization angles are obtained from the Stokes Q and U values using Equation (6) and sampled on a 12'' grid, similar to the beam size of the observations. Half-vectors are plotted where (1) $I/\delta I > 10$, (2) $\text{PI}/\delta \text{PI} > 3$, and (3) $\delta P < 5\%$. The length of each vector indicates its polarization fraction. The right panel of Figure 2 shows the magnetic field morphology of the IC 348 star-

forming region. Magnetic field orientations are inferred by rotating the observed polarization angles by 90°, assuming that the major axis of nonspherical dust grains is perpendicular to local magnetic fields (e.g., B. G. Andersson et al. 2015).

To study the relationship between magnetic fields and the filamentary structure of the region, we measure angles between magnetic field orientations and filament directions. We first found a filament skeleton using the *filfinder* package (E. W. Koch & E. W. Rosolowsky 2015), with a size threshold of 200 square pixels. The extracted filament skeleton is shown in the left panel of Figure 3. Then, we derived the Hessian matrix of the 850 μm intensity map to determine the filament directions in each skeleton pixel. Since the Hessian matrix is a second-order partial derivative of a scalar function, it provides information about the curvature of the scalar function near any given point. Thus, by deriving the Hessian matrix of the intensity field, the two eigenvectors at any given position are directly related to the intensity contrast at that point. Before deriving the Hessian matrix, we convolved the intensity map with a Gaussian 2D kernel with a standard deviation of 16'' to make a smoothed map, since smoothing through a Gaussian function of an order of the instrumental beam effectively suppresses pixel-to-pixel noise levels while minimizing blurring of the filamentary structures (E. Schisano et al. 2014). A pair of eigenvectors of the Hessian matrix at skeleton pixels are derived, and the filament direction is accepted to be the eigenvector direction with the smaller eigenvalue. For detailed descriptions of a filament direction identification, refer to E. Schisano et al. (2014). The right panel of Figure 3 shows the filament directions at each skeleton pixel. The displayed angles are measured positively from north to east in the equatorial frame, ranging from -90 to 90° . Then, we matched observed magnetic field segments with the nearest filament skeleton pixels and measured the angle between the magnetic field orientation of the segment and the filament direction of the nearest pixel. In this process, the angles were accepted when the distance between a magnetic field segment and the nearest skeleton pixel is smaller than 30'', which corresponds to about 0.043 pc.

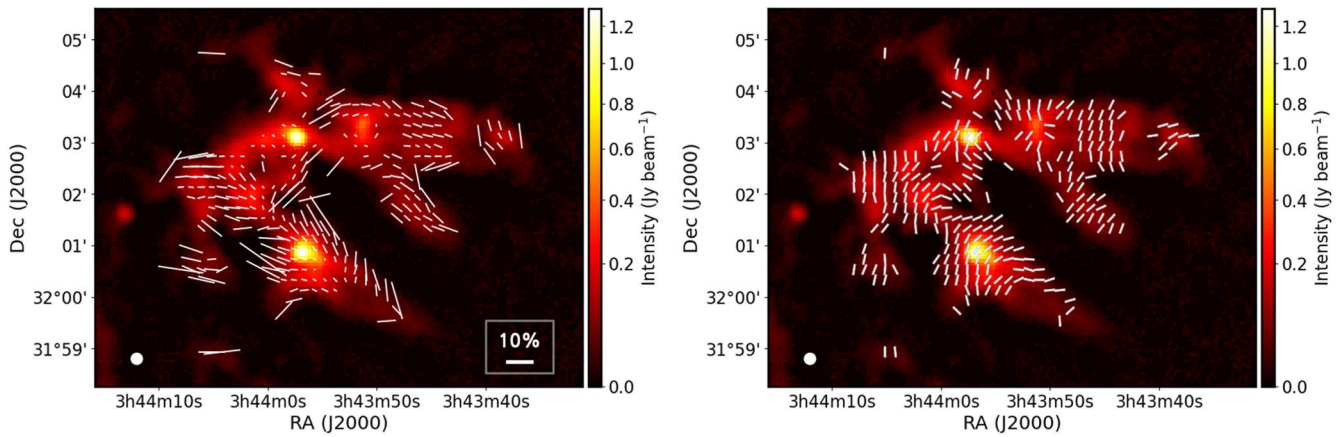


Figure 2. Left: linear polarization angles and fractions in the IC 348 star-forming region detected in $850\ \mu\text{m}$ dust continuum. The length of each segment is proportional to the polarization fraction, and the reference length is shown in the lower right corner. Right: magnetic field orientations in the IC 348 star-forming region obtained by 90° rotations of the linear polarization angles. Segment lengths are uniform to have the field directions better presented. The background image is the $850\ \mu\text{m}$ total intensity, and the beam size is shown in the lower left corner of both panels.

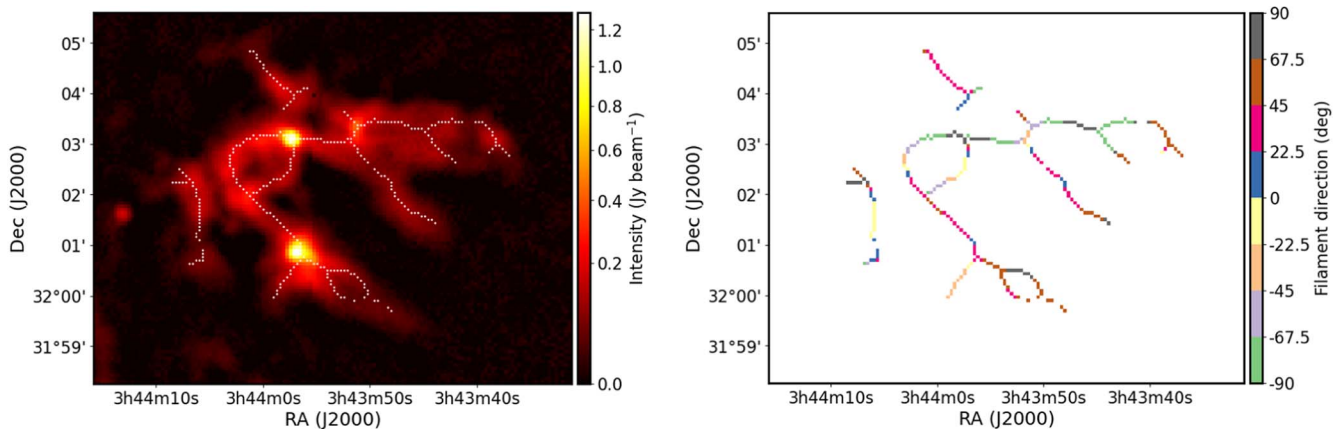


Figure 3. Left: filament skeleton of the IC 348 star-forming region. Right: position angles of the filament at individual positions of the filament skeleton.

The relative orientations between the filament and magnetic fields at the locations of observed magnetic field segments can be seen in the left panel of Figure 4. Red circles represent the points where the measured angle is larger than 50° (perpendicular-like). In contrast, blue circles represent where the measured angle is smaller than 40° (parallel-like). Yellow circles are the points between 40° and 50° . We applied rough criteria for identifying perpendicular-like and parallel-like data points, given that the measured angles are based on plane-of-sky projections. For example, even if the magnetic field and a filament are orthogonal in 3D space, the projected angles between them could be significantly less than 90° , depending on the inclination; see Section 5.2 of Y. Doi et al. (2020). The right panel of Figure 4 shows the distribution of the measured angles between the filament and magnetic field of the region. There are more cases close to the perpendicular orientation than close to the parallel one.

Note that the relative angles between magnetic fields and the filament here are based on projected directions. Real relative angles in the 3D space could differ from the projected angles (Y. Doi et al. 2020, 2021). Figure 5 shows the cumulative distribution function (CDF) of the projected angles between the magnetic fields and the filament. To show expected CDFs of projected angles between magnetic fields and filaments, we generated vectors in 3D space, projected

them into the plane of the sky, and constructed distributions of projected angles between two vectors, following the method given by I. W. Stephens et al. (2017). The observed CDF is qualitatively well fitted with the CDF when real 3D angles are distributed between 45° and 80° . This result indicates that the magnetic field orientations in IC 348 are not random and are closer to a perpendicular configuration than a parallel one, even though the observed CDF does not perfectly match the CDF for 3D angles ranging from 70° to 90° . It is important to note that the observed magnetic field orientations and the filament directions in IC 348 might result from a projection in a particular direction. In contrast, the expected CDFs are based on random projections. Detailed studies with modeling for 3D structures of the magnetic fields and the filament are beyond the scope of this paper (e.g., M. Tahani et al. 2022; M. Tahani 2022).

Figure 6 shows the magnetic field orientations of the two core regions sampled on $8''$ intervals. The mean field orientations are 147° for HH 211 MMS and 153° for IC 348 MMS within the defined core regions. The observed magnetic fields and outflow directions are relatively well aligned at the two core regions, even though previous statistical studies show that, in general, most outflows and magnetic field directions are randomly distributed (C. L. H. Hull & Q. Zhang 2019; Y. Doi et al. 2020) or misaligned by 50° (H.-W. Yen et al. 2021).

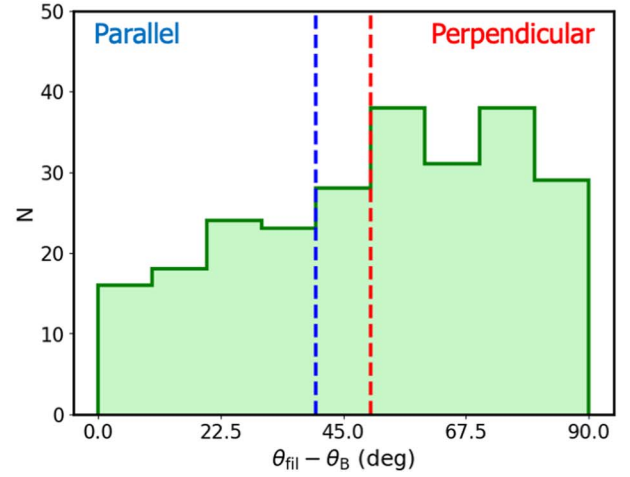
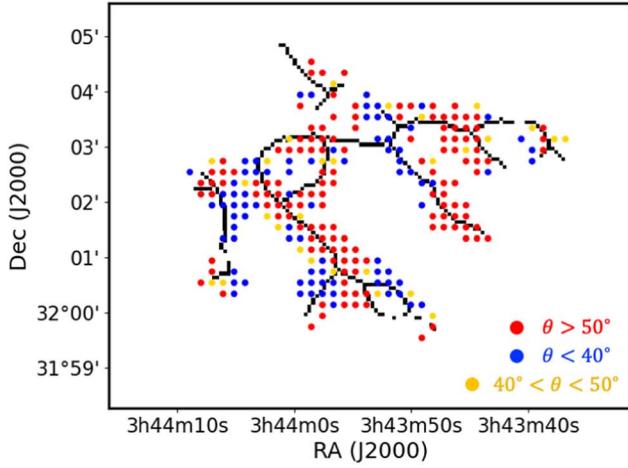


Figure 4. Left: the relation between the filament and magnetic fields at each location of the half-vectors. Red circles represent perpendicular-like points ($\theta > 50^\circ$), while blue circles represent parallel-like points ($\theta < 40^\circ$). Yellow circles represent neither perpendicular-like nor parallel-like ($40^\circ < \theta < 50^\circ$). Right: histogram of the measured angles between the filament and magnetic fields of the IC 348 star-forming region. Blue and red dashed lines represent 40° and 50° , respectively.

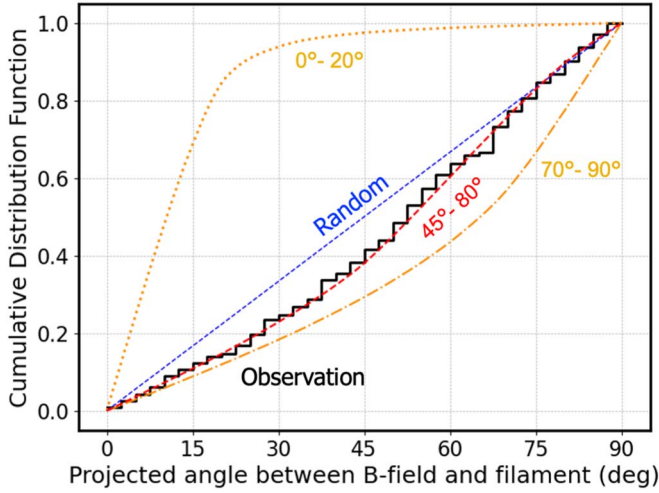


Figure 5. CDF of projected angles between magnetic fields and filaments. The black line shows the CDF of observed projected angles between magnetic fields and the filament. Orange lines indicate expected CDFs when 3D angles are from 0° to 20° and from 70° to 90° , respectively. The blue line represents when magnetic fields and filaments are randomly oriented. The red line shows the qualitatively best-fit case (45° – 80°).

4. Polarization Fraction versus Intensity

The general trend of declining polarization efficiency with increased intensity in molecular clouds is well described by the power-law dependence of polarization fraction with intensity, $P \propto I^{-\alpha}$ (D. C. B. Whittet et al. 2008). Perfect grain alignment results in $\alpha = 0$, while $\alpha = 1$ indicates that all polarization is due to the alignment of dust grains only on the surface of molecular clouds, and there is no polarization inside the clouds. If grain alignment decreases with increasing density, the power index α lies between 0 and 1 (D. C. B. Whittet et al. 2008; T. J. Jones et al. 2015).

We studied the power-law dependence of polarization fraction on intensity using both the single power-law model and the Ricean-mean method, as described by K. Pattle et al. (2019). The single power-law relation between polarization fraction and intensity is given by

$$P_{\text{debiased}} = p_{\sigma_{QU}} \left(\frac{I}{\sigma_{QU}} \right)^{-\alpha}, \quad (8)$$

where σ_{QU} is the rms noise in both the Stokes Q and U maps and $p_{\sigma_{QU}}$ represents the polarization fraction at the noise level of the data. If both the Stokes Q and U follow Gaussian distributions, non-debiased PI ($\sqrt{Q^2 + U^2}$) is mathematically Rice distributed. Rice distributions exhibit positive skewness with low-S/N Stokes Q and U data, while approaching a Gaussian distribution in the high-S/N limit. K. Pattle et al. (2019) proposed the mean of the Rice distribution method to recover the α index, and we follow Equation (21) of K. Pattle et al. (2019). Their Monte Carlo simulations showed that the Ricean-mean method can accurately recover α values up to $\alpha \sim 0.6$. In contrast, the power-law method tends to overestimate α values since low-S/N data points skew α toward 1 owing to statistical noise. Even moderate-S/N selection criteria tend to bias α values, as significant S/N is needed to distinguish between true power-law behavior and noise effects. For detailed descriptions, refer to K. Pattle et al. (2019).

We applied a power-law fit and Ricean-mean method to the two cores and the filament. The fitting areas of the two cores are shown as black dashed lines in Figure 7. For the filament, the whole region except the two black dashed areas is used for the fittings. In the power-law method, we used data points with $I/\delta I > 10$, $PI/\delta PI > 3$, and $\delta P < 5\%$, whereas all data points within the fitting areas were used when applying the Ricean-mean method. We set σ_{QU} to be the mean value of uncertainties in the Stokes Q and U maps, as suggested by K. Pattle et al. (2019). To find the values of $p_{\sigma_{QU}}$ and α , we adopted a Markov Chain Monte Carlo sampling. Flat priors were used for both values, α was restricted to be between 0 and 1, and $p_{\sigma_{QU}}$ was restricted to be positive.

Figure 8 shows the best-fit results from the power law and the mean of the Rice distribution methods, and the recovered $p_{\sigma_{QU}}$ and α values are summarized in Table 1. The uncertainties of individual parameters are based on the 16th and 84th percentiles of the sample distributions. In all cases, the Ricean-mean method gives smaller α values as expected by K. Pattle et al. (2019), which supports the argument that the power-law method could overestimate α values in comparison with the Ricean-mean method. Therefore, we adopt the results from the Ricean-mean method.

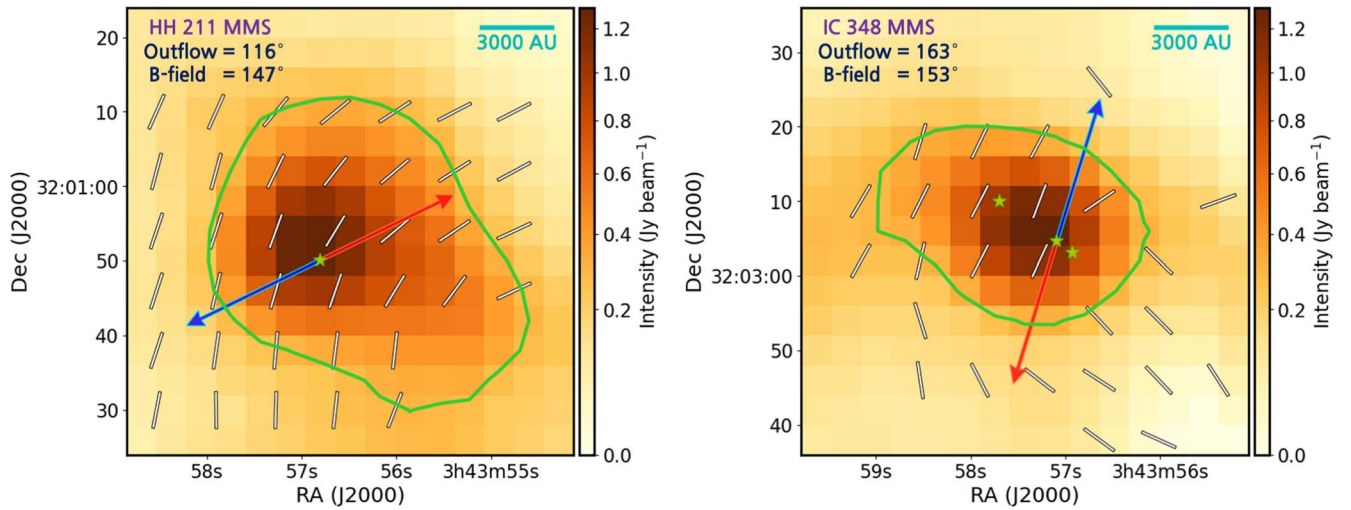


Figure 6. The magnetic field orientations of HH 211 MMS (left) and IC 348 MMS (right). Green lines are at total intensity of 0.3 Jy beam^{-1} , indicative of the core regions. Red and blue lines represent redshifted and blueshifted outflow directions, respectively (L. F. Rodríguez et al. 2014), and stellar markers indicate the locations of protostars in the two cores (L. F. Rodríguez et al. 2014).

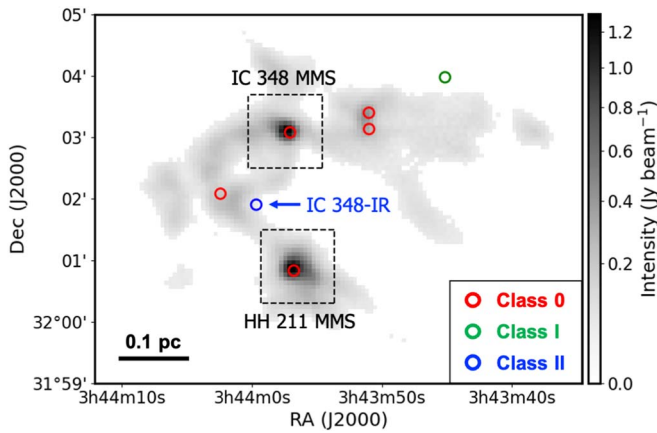


Figure 7. Positions of young stellar objects in IC 348 from the VANDAM survey (J. J. Tobin et al. 2016) are marked by circles: red, green, and blue ones for Class 0, I, and II sources, respectively. The black dashed squares show the area of HH 211 MMS and IC 348 MMS where the power-law and Ricean-mean fittings are carried out. Bright IR source IC 348-IR is located between HH 211 MMS and IC 348 MMS (S. E. Strom et al. 1974; M. J. McCaughrean et al. 1994). The background in gray is the $850 \mu\text{m}$ intensity.

The power indices obtained by the Ricean-mean method are 0.59, 0.30, and 0.34 for the filament, HH 211 MMS, and IC 348 MMS, respectively. These results indicate that a significant fraction of dust grains should be aligned with the magnetic field even in the high-density regions, justifying the use of polarization observations to infer the magnetic field properties of the area. Furthermore, it is noticeable that the power indices of the two cores are smaller than that of the filament. This result implies that some mechanisms effectively align dust grains in high-density regions of the cores.

5. Magnetic Field Strength

In this section, we estimate the magnetic field strength in the IC 348 star-forming region using the Davis–Chandrasekhar–Fermi (DCF; L. Davis 1951; S. Chandrasekhar & E. Fermi 1953) method and its alternative version for compressed medium (ST method; R. Skalidis & K. Tassis 2021). The DCF method assumes that turbulence collectively shakes the aligned dust

grains, thereby distorting the polarization direction. If magnetic fields are strong enough, the magnetic fields are little distorted, whereas if magnetic fields are weak, they are disturbed significantly. Therefore, it is possible to estimate the magnetic field strength by measuring the degree of dispersion in magnetic field orientations.

There have been numerous efforts to modify and refine the DCF method to estimate the magnetic field strength accurately (e.g., R. H. Hildebrand et al. 2009; M. Houde et al. 2009; J. Cho & H. Yoo 2016; R. Skalidis & K. Tassis 2021). One example is the ST method (R. Skalidis & K. Tassis 2021). R. Skalidis & K. Tassis (2021) pointed out that DCF assumes incompressible fluids and ignores the compressible modes. Since the ISM is highly compressible, the DCF assumption may not be generally applicable and may lead to an inaccurate estimation of field strengths. Thus, they proposed an alternative method containing the presence of compressible turbulence. However, it is claimed that the ST method also contains uncertainties, and interpretation of this method should also be done with caution (A. Lazarian et al. 2022; P. S. Li et al. 2022; J. Liu et al. 2022). Detailed studies with the physical interpretation of the DCF method and its various modified versions are beyond the scope of this paper (e.g., A. Lazarian et al. 2022; J. Liu et al. 2022). In this paper, we applied both DCF and ST methods to provide a range of results from them.

The equations of DCF and ST methods are as follows:

$$B_{\text{pos}} = f \sqrt{4\pi\rho} \frac{\delta v}{\delta\theta} \quad (\text{DCF}), \quad (9)$$

$$B_{\text{pos}} = \sqrt{4\pi\rho} \frac{\delta v}{\sqrt{2\delta\theta}} \quad (\text{ST}), \quad (10)$$

where ρ is the gas mass density, δv is the velocity dispersion, and $\delta\theta$ is the dispersion in polarization angles representing magnetic field orientations.

DCF has a correcting factor f , which is commonly used for modifying the original DCF method. A. Lazarian et al. (2022) pointed out that the correcting factor depends on the properties of the turbulence. J. Liu et al. (2022) also argued that the correcting factor decreases as the density of the region increases based on the results of three independent simulations

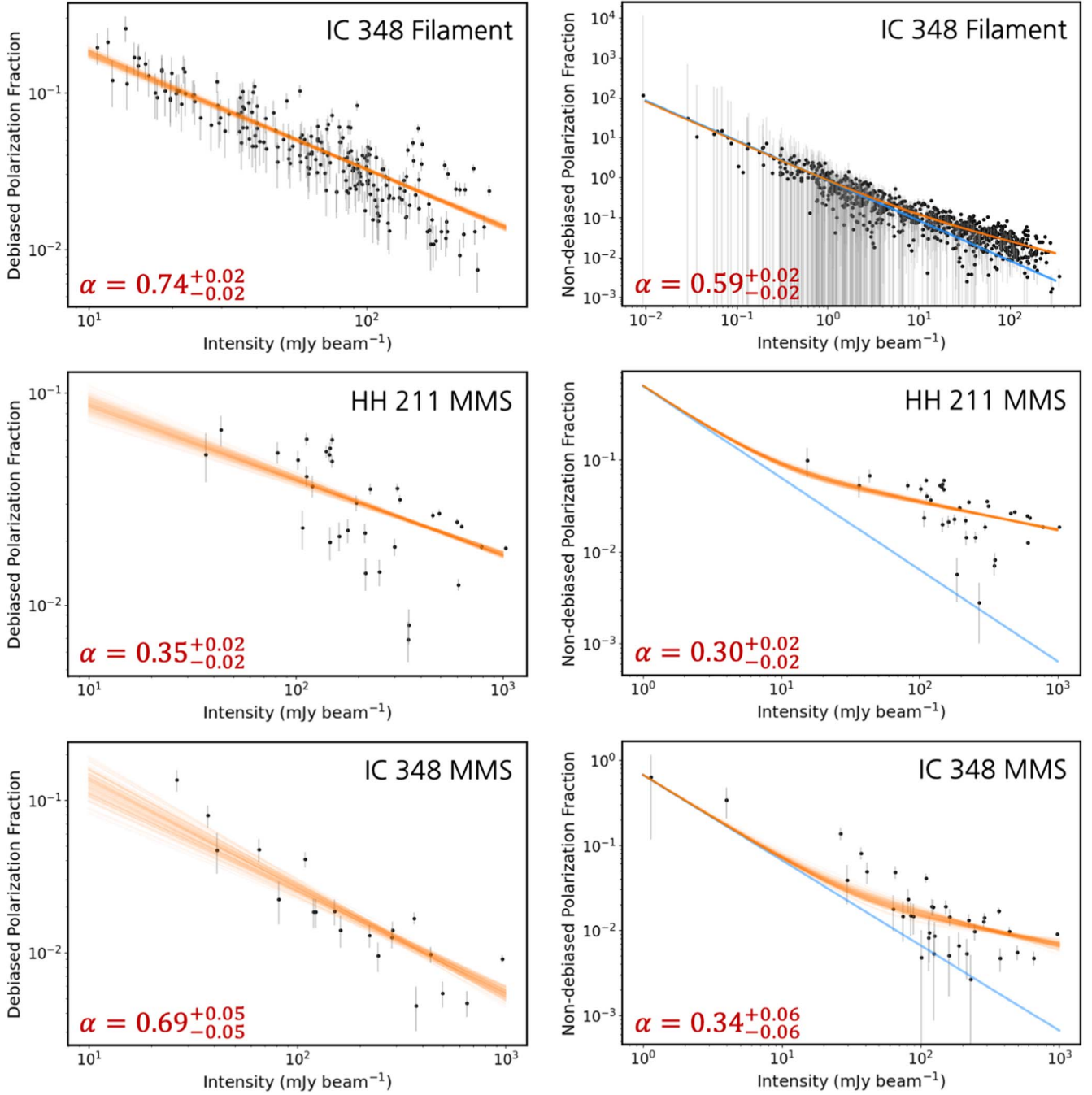


Figure 8. Left: debiased polarization fraction vs. total intensity at $850 \mu\text{m}$ in the filament (top), HH 211 MMS (middle), and IC 348 MMS (bottom). Only data points with $I/\delta I > 10$, $PI/\delta PI > 3$, and $\delta P < 5\%$ are selected and are fitted with the power-law model. Orange lines represent 100 random draws from the posterior distribution. Right: non-biased polarization fraction vs. total intensity at $850 \mu\text{m}$ in the filament (top), HH 211 MMS (middle), and IC 348 MMS (bottom). All data points within the defined areas are selected and are fitted with the Ricean-mean model. Orange lines represent 100 random draws from the posterior distribution, while the blue lines indicate the case of $\alpha = 1$. The best-fit alpha values are indicated in the lower left corner of each panel.

Table 1
Fitted $p_{\sigma QU}$ and α Values in P versus I Relations

Method	Description	HH		
		Filament	211 MMS	IC 348 MMS
Power law	$p_{\sigma QU}$	$1.50^{+0.16}_{-0.14}$	$0.26^{+0.03}_{-0.03}$	$0.98^{+0.35}_{-0.26}$
	α	$0.74^{+0.02}_{-0.02}$	$0.35^{+0.02}_{-0.02}$	$0.69^{+0.05}_{-0.05}$
Mean of the Rice distribution	$p_{\sigma QU}$	$0.48^{+0.04}_{-0.04}$	$0.17^{+0.02}_{-0.02}$	$0.09^{+0.04}_{-0.03}$
	α	$0.59^{+0.02}_{-0.02}$	$0.30^{+0.02}_{-0.02}$	$0.34^{+0.06}_{-0.06}$

(E. C. Ostriker et al. 2001; P. Padoan et al. 2001; J. Liu et al. 2021). In this paper, we applied $f=0.5$, which is commonly used.

To apply the DCF and ST methods to our target, we converted Equations (9) and (10) into the formulations given by R. M. Crutcher et al. (2004) as follows:

$$B_{\text{pos}}(\mu\text{G}) \approx 9.42 \sqrt{n(\text{H}_2)(\text{cm}^{-3})} \frac{\Delta V(\text{km s}^{-1})}{\sigma_{\theta}(\text{deg})} \quad (\text{DCF}), \quad (11)$$

$$B_{\text{pos}}(\mu\text{G}) \approx 1.76 \sqrt{n(\text{H}_2)(\text{cm}^{-3})} \frac{\Delta V(\text{km s}^{-1})}{\sqrt{\sigma_\theta(\text{deg})}} \quad (\text{ST}), \quad (12)$$

where $n(\text{H}_2)$ is the number density of hydrogen molecules, ΔV is the FWHM velocity dispersion, σ_θ is the angular dispersion in polarization angles, and B_{pos} is the plane-of-sky magnetic field strength. We adopt $f=0.5$ in the DCF analysis. Using Equations (11) and (12), we measured the magnetic field strengths of the two core regions and the filament defined in Figure 1 and studied the roles of magnetic fields in both core (~ 0.05 pc) and filament scales (~ 0.5 pc). The results are summarized in Table 2.

5.1. Angular Dispersion of Polarization

We constructed the observed polarization angle map using the Stokes Q and U maps with Equation (6). Then, to make a background large-scale polarization map, we applied the unsharp masking method (K. Pattle et al. 2017a), which smooths the Q and U maps with the 3×3 boxcar kernel. Since a larger boxcar filter could overly smooth the nonturbulent magnetic field curvature of the filament, we chose a 3×3 boxcar filter, corresponding to a length of 0.05 pc, which is comparable to half of the typical filament's width (P. André et al. 2014). Subtracting the background polarization map from the original polarization angle map provides residual polarization angles:

$$\Delta\theta = \theta_{\text{data}} - \theta_{\text{bg}}, \quad (13)$$

where θ_{data} and θ_{bg} represent the observed and smoothed polarization angles, respectively, while $\Delta\theta$ indicates the residual angles. To calculate the angular dispersion of the three different regions defined above, we cropped the residual map into individual areas and estimated the dispersion from each cropped residual angle map. In this process, the polarization angles in core regions are sampled on an $8''$ grid.

Figure 9 shows the distributions of $\Delta\theta$ in HH 211 MMS, IC 348 MMS, and the filament. We fitted a Gaussian function to each distribution and adopted its standard deviation as the angular dispersion of each area. For IC 348 MMS, instead of the Gaussian fitting, the standard deviation of the distribution is adopted owing to the lack of data points. The angular dispersions of HH 211 MMS, IC 348 MMS, and the filament are $7.^\circ 6 \pm 0.^\circ 1$, $9.^\circ 8$, and $13.^\circ 5 \pm 0.^\circ 7$, respectively.

5.2. Number Density

Number densities are determined from 450 μm and 850 μm intensity maps observed by SCUBA-2. We applied a Gaussian convolution to the 450 μm intensity map to match the angular resolution to the 850 μm intensity map. We assumed that dust continuum in IC 348 is optically thin at both wavelengths. The observed intensity in optically thin cases is given by

$$\begin{aligned} I_\nu &= \tau_\nu B_\nu(T) \\ &= \kappa(\nu) \Sigma_d B_\nu(T) \\ &= \mu m_{\text{H}} \kappa(\nu) N(\text{H}_2) B_\nu(T), \end{aligned} \quad (14)$$

where I_ν is the intensity at a frequency ν , τ_ν is the optical depth, Σ_d is the mass column density, μ is the mean molecular weight of the molecular cloud, m_{H} is the mass of a hydrogen atom, $\kappa(\nu)$ is the dust mass absorption coefficient at frequency ν

(R. H. Hildebrand 1983), $N(\text{H}_2)$ is the column density of molecular hydrogen, and $B_\nu(T)$ is the blackbody radiation at dust temperature T . We adopted $\mu = 2.86$, assuming that the proportion of hydrogen in gas mass is 70% (J. M. Kirk et al. 2013).

The dust opacity function is as follows:

$$\kappa(\nu) = \kappa_{\nu_0} \left(\frac{\nu}{\nu_0} \right)^\beta, \quad (15)$$

where κ_{ν_0} is the dust opacity at a frequency ν_0 and β is a dust opacity spectral index. We take a β value of 1.7 (e.g., Y. Lin et al. 2016), and $\kappa_{\nu_0} = 0.1 \text{ cm}^2 \text{ g}^{-1}$ at $\nu_0 = 1$ THz, assuming a gas-to-dust mass ratio of 100 (S. V. W. Beckwith & A. I. Sargent 1991).

To measure the column density and dust temperature of the target region, we follow the method given by K. Pattle et al. (2017b). We divided the 850 μm intensity map by the 450 μm intensity map using Equation (14). Then, the column density term is eliminated, leaving only the temperature-related equation as

$$\frac{I_{850}}{I_{450}} = \left(\frac{\nu_{850}}{\nu_{450}} \right)^{3+\beta} \left(\frac{e^{\frac{h\nu_{450}}{k_{\text{B}}T}} - 1}{e^{\frac{h\nu_{850}}{k_{\text{B}}T}} - 1} \right). \quad (16)$$

We solved Equation (16) to measure the dust temperature. Then, we inferred the column density of each pixel using Equation (14). Figure 10 shows the estimated dust temperature and column density of IC 348. Dust temperature is high near the young stellar objects, especially near IC 348-IR marked in Figure 7. Two core regions have column densities greater than 10^{23} cm^{-2} at their central areas, and the filamentary structure has a column density scale of 10^{22} cm^{-2} .

The column densities of HH 211 MMS, IC 348 MMS, and the filament are obtained by averaging the pixel values of the defined areas. We calculated the uncertainty in the inferred column density by applying error propagation through Equations (14)–(16). We assumed that the uncertainty on the reference dust opacity κ_{ν_0} is 50% (A. Roy et al. 2014) and the uncertainty of the dust opacity spectral index β is ± 0.3 (S. I. Sadavoy et al. 2013, 2016). Uncertainties in 450 μm and 850 μm intensities are about 15% and 6%, respectively (S. Mairs et al. 2021). When considering these uncertainties, the systematic uncertainty in calculated column densities is about 67%. Consequently, the measured column densities of each area are as follows: $N(\text{H}_2) = (4.1 \pm 2.9) \times 10^{22} \text{ cm}^{-2}$, $(6.2 \pm 4.1) \times 10^{22} \text{ cm}^{-2}$, and $(9.2 \pm 6.2) \times 10^{21} \text{ cm}^{-2}$ for HH 211 MMS, IC 348 MMS, and the filament, respectively.

For calculating number densities of the region, we assumed that the line-of-sight depth of the cloud is equal to the width of the filament. We calculated the width of the filament, which is 0.050 pc, by dividing the defined filament area (Figure 1) by the length of the filament skeleton in the left panel of Figure 3. The number density $n(\text{H}_2)$ is estimated through

$$n(\text{H}_2) = \frac{N(\text{H}_2)}{W}, \quad (17)$$

where $N(\text{H}_2)$ is the column density and W is the width or line-of-sight depth of the region. Assuming that the uncertainty of the width is 50%, the measured number densities of HH 211 MMS, IC 348 MMS, and the filament are $n(\text{H}_2) = (2.7 \pm 2.3) \times$

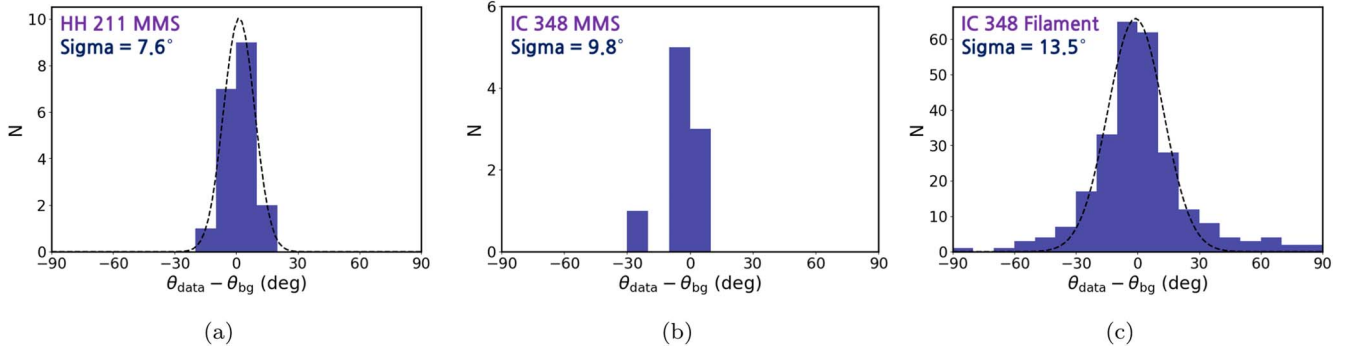


Figure 9. Residual polarization angle ($\Delta\theta$) distributions of (a) HH 211 MMS, (b) IC 348 MMS, and (c) the filament. The dashed lines are the fitted Gaussian functions, whose sigmas are shown in each panel. For IC 348 MMS, the standard deviation of the distribution is adopted as the angular dispersion of the region.

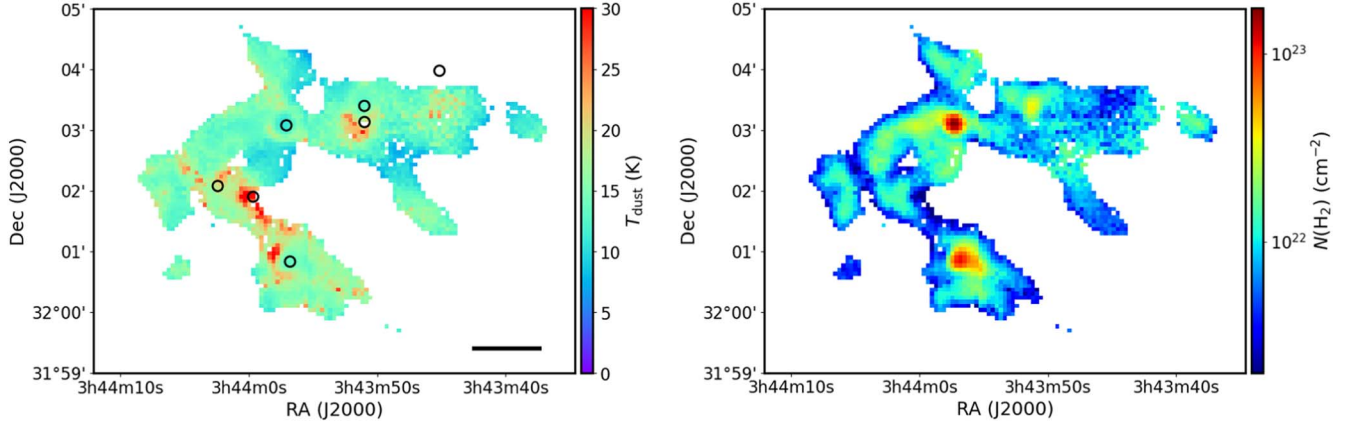


Figure 10. The estimated dust temperature (left) and column density (right) maps of the IC 348 star-forming region. The black circles in the left panel indicate the positions of young stellar objects, as in Figure 7.

10^5 cm^{-3} , $(4.0 \pm 3.3) \times 10^5 \text{ cm}^{-3}$, and $(6.0 \pm 5.1) \times 10^4 \text{ cm}^{-3}$, respectively.

5.3. Velocity Dispersion

Average velocity dispersions in IC 348 are calculated from the $\text{C}^{18}\text{O } J=3 \rightarrow 2$ observations made using HARP (J. V. Buckle et al. 2009). The left panel of Figure 11 shows that C^{18}O emission is spatially well correlated with the dust continuum. To measure C^{18}O velocity dispersion, we fitted a Gaussian profile to a C^{18}O spectrum of each pixel and accepted the Gaussian width as the C^{18}O velocity dispersion of the pixel. We measured the average velocity dispersion over the pixels within the defined areas to calculate the C^{18}O velocity dispersion of the two cores and the filament. Measured C^{18}O velocity dispersions for HH 211 MMS, IC 348 MMS, and the filament are $\sigma_{v, \text{C}^{18}\text{O}} = 0.27 \pm 0.04 \text{ km s}^{-1}$, $0.30 \pm 0.04 \text{ km s}^{-1}$, and $0.26 \pm 0.07 \text{ km s}^{-1}$, respectively.

From the C^{18}O velocity dispersion, we estimated the nonthermal velocity dispersion by removing the thermal component:

$$\sigma_v^2 = \sigma_{v, \text{C}^{18}\text{O}}^2 - \frac{k_B T}{m_{\text{C}^{18}\text{O}}}, \quad (18)$$

where σ_v is the nonthermal velocity dispersion, $\sigma_{v, \text{C}^{18}\text{O}}$ is the total velocity dispersion of C^{18}O , $m_{\text{C}^{18}\text{O}} = 30 \text{ amu}$ (the mass of the C^{18}O molecule), k_B is the Boltzmann constant, and T is the gas temperature. Assuming that the gas temperature is the same as the dust temperature, the gas temperature values for the

thermal motion were obtained by averaging the estimated dust temperatures in the defined areas. They are $16.2 \pm 6.0 \text{ K}$, $13.4 \pm 3.9 \text{ K}$, and $14.8 \pm 4.9 \text{ K}$ at HH 211 MMS, IC 348 MMS, and the filament, respectively.

Finally, we derived nonthermal velocity dispersions of $\sigma_v = 0.26 \pm 0.04 \text{ km s}^{-1}$, $0.29 \pm 0.04 \text{ km s}^{-1}$, and $0.25 \pm 0.07 \text{ km s}^{-1}$ for HH 211 MMS, IC 348 MMS, and the filament, respectively. These correspond to velocity FWHMs of $\Delta V = 0.62 \pm 0.09 \text{ km s}^{-1}$, $0.68 \pm 0.10 \text{ km s}^{-1}$, and $0.60 \pm 0.18 \text{ km s}^{-1}$.

5.4. Magnetic Field Strength

Using Equations (11) and (12), we determined magnetic field strengths of the two cores and the filament. Table 2 lists the field strengths from the DCF and ST methods. The results from the DCF analysis are $B_{\text{pos}} = 394 \pm 170 \mu\text{G}$, $417 \pm 182 \mu\text{G}$, and $102 \pm 52 \mu\text{G}$ for HH 211 MMS, IC 348 MMS, and the filament, respectively. The respective magnetic field strengths using the ST method are $B_{\text{pos}} = 203 \pm 87 \mu\text{G}$, $244 \pm 106 \mu\text{G}$, and $70 \pm 35 \mu\text{G}$.

The mass-to-flux ratio λ is defined in units of the critical value, which is inferred using the equation below, given by R. M. Crutcher et al. (2004):

$$\lambda = 7.6 \times 10^{-21} \frac{N(\text{H}_2)(\text{cm}^{-2})}{B_{\text{pos}}(\mu\text{G})}. \quad (19)$$

This parameter is used to measure the relative importance between gravity and magnetic field in molecular clouds (T. Nakano & T. Nakamura 1978). When $\lambda > 1$ (magnetically

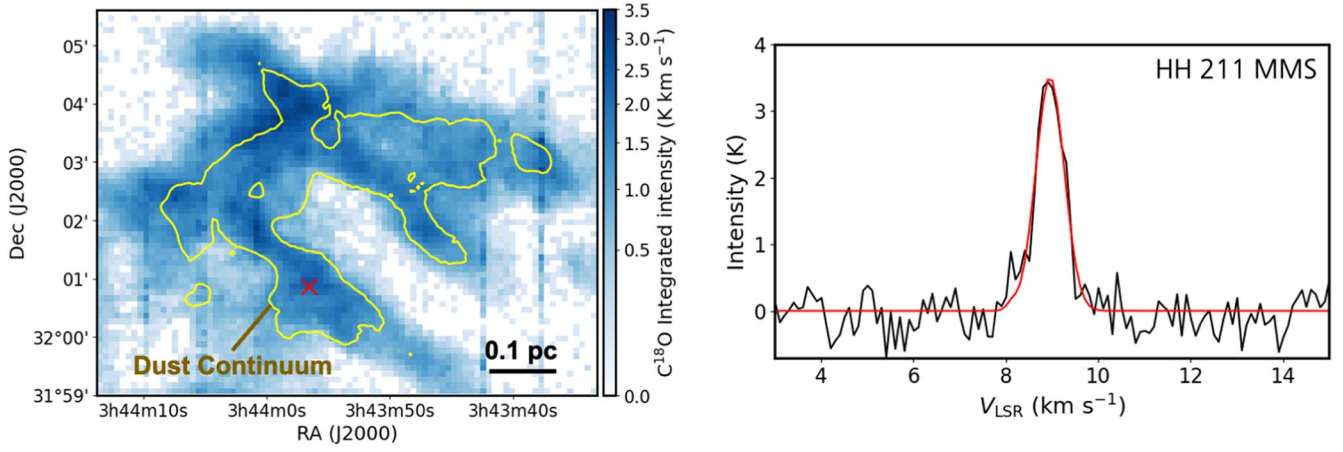


Figure 11. Left: the integrated intensity map of the $\text{C}^{18}\text{O } J = 3 \rightarrow 2$ emissions. The yellow contour indicates the $850 \mu\text{m}$ dust continuum at the $0.05 \text{ Jy beam}^{-1}$ level. The red cross shows the position of the spectrum shown in the right panel. Right: an example C^{18}O spectral line toward HH 211 MMS. The observed spectrum and its Gaussian fitting result are shown as the black and red lines, respectively.

supercritical), gravity dominates over the magnetic field. In contrast, $\lambda < 1$ (magnetically subcritical) indicates that the magnetic field is strong enough to prevent gravitational collapse.

The mass-to-flux ratios based on the magnetic field strengths of both the DCF and ST methods are given in Table 2. For the DCF method, we find values of $\lambda = 0.79 \pm 0.34$, 1.12 ± 0.49 , and 0.68 ± 0.35 for HH 211 MMS, IC 348 MMS, and the filament, respectively. With the ST method, the respective ratios are $\lambda = 1.54 \pm 0.66$, 1.92 ± 0.84 , and 1.00 ± 0.50 . The core regions have larger λ values than the filament. These results suggest that the cores are likely to be magnetically supercritical or in balance, while the filament is likely to be magnetically subcritical. Note that the observed mass-to-flux ratios may overestimate the true values since only the plane-of-sky magnetic field components are considered (R. M. Crutcher et al. 2004). Here we did not apply geometric corrections to the observed mass-to-flux ratios, due to lack of line-of-sight magnetic field information.

6. Energy Balance in the Core Regions

The interplay between gravity, thermal pressure, turbulence, and magnetic fields plays a role in the star formation process. Therefore, it is vital to probe the energy balance of molecular clouds at different scales to understand the interaction between various factors. In this section, we measure (1) magnetic energies, (2) gravitational energies, (3) thermal energies, and (4) turbulent energies in HH 211 MMS and IC 348 MMS and compare the relative importance between them. The results are summarized in Table 3.

The magnetic energy is calculated as

$$E_B = \frac{B^2}{8\pi} V \quad (20)$$

in cgs units, where V is the region's volume and B is the magnetic field strength. We assumed that the cores are a sphere whose radius is that of a circle with the same area as the core. The measured radii are 0.029 and 0.022 pc for HH 211 MMS and IC 348 MMS, respectively. When adopting the DCF magnetic field strengths, the inferred magnetic energies are $E_B = (1.8 \pm 1.6) \times 10^{43}$ erg in HH 211 MMS and $(8.8 \pm 7.7) \times 10^{42}$ erg in IC 348

MMS. The ST field strengths result in $E_B = (4.8 \pm 4.1) \times 10^{42}$ erg for HH 211 MMS and $(3.0 \pm 2.6) \times 10^{42}$ erg for IC 348 MMS.

The gravitational energy of a uniform sphere is given by

$$E_G = -\frac{3}{5} \frac{GM^2}{R}, \quad (21)$$

where R is the radius and M is the mass of the sphere. Mass can be estimated from the dust thermal emission by the following equation (e.g., R. H. Hildebrand 1983; W. Kwon et al. 2009):

$$M = \frac{F_\nu D^2}{\kappa_\nu B_\nu(T)}, \quad (22)$$

where F_ν is the total flux, D is the distance, κ_ν is the opacity, and B_ν is blackbody radiation. The masses are estimated as $(2.45 \pm 1.57) M_\odot$ for HH 211 MMS and $(2.09 \pm 1.25) M_\odot$ for IC 348 MMS. These correspond to gravitational energies of $E_G = (-1.1 \pm 1.4) \times 10^{43}$ erg and $(-1.0 \pm 1.2) \times 10^{43}$ erg for HH 211 MMS and IC 348 MMS, respectively. Note that the estimated gravitational energies from Equation (21) are lower limits (in absolute value), since the mass is expected to be concentrated near the center of the cores.

The thermal energy is calculated as

$$E_{\text{thermal}} = \frac{3}{2} M c_s^2, \quad (23)$$

where c_s is the sound speed in the gas:

$$c_s = \sqrt{\frac{k_B T}{\mu m_H}}. \quad (24)$$

The gas temperature is assumed to be the same as the dust temperature. Using the estimated masses and dust temperatures of the core regions, thermal energies are calculated to be $E_{\text{thermal}} = (3.4 \pm 2.5) \times 10^{42}$ erg for HH 211 and $(2.4 \pm 1.6) \times 10^{42}$ erg for IC 348 MMS.

The turbulent energy or nonthermal kinetic energy is calculated as

$$E_{\text{non-thermal}} = \frac{3}{2} M \sigma_v^2, \quad (25)$$

Table 2
The Measured Properties for Estimating the Magnetic Field Strengths in the IC 348 Star-forming Region

Parameter	Description	HH 211 MMS	IC 348 MMS	Filament
σ_θ	Angular dispersion	$7.6 \pm 0.9^\circ$	9.8	13.95 ± 0.97
$N(\text{H}_2)$	Hydrogen column density	$(4.1 \pm 2.9) \times 10^{22} \text{ cm}^{-2}$	$(6.2 \pm 4.1) \times 10^{22} \text{ cm}^{-2}$	$(9.2 \pm 6.2) \times 10^{21} \text{ cm}^{-2}$
$n(\text{H}_2)$	Hydrogen number density	$(2.7 \pm 2.3) \times 10^5 \text{ cm}^{-3}$	$(4.0 \pm 3.3) \times 10^5 \text{ cm}^{-3}$	$(6.0 \pm 5.1) \times 10^4 \text{ cm}^{-3}$
T_{dust}	Dust temperature	$16.2 \pm 6.0 \text{ K}$	$13.4 \pm 3.9 \text{ K}$	$14.8 \pm 4.9 \text{ K}$
M	Mass	$2.45 \pm 1.57 M_\odot$	$2.09 \pm 1.25 M_\odot$	$16.09 \pm 9.95 M_\odot$
R, W	Radius, width	0.029 pc	0.022 pc	0.050 pc
σ_v	Nonthermal velocity dispersion	$0.26 \pm 0.04 \text{ km s}^{-1}$	$0.29 \pm 0.04 \text{ km s}^{-1}$	$0.25 \pm 0.07 \text{ km s}^{-1}$
ΔV	Velocity FWHM	$0.62 \pm 0.09 \text{ km s}^{-1}$	$0.68 \pm 0.10 \text{ km s}^{-1}$	$0.60 \pm 0.18 \text{ km s}^{-1}$
$B_{\text{pos,DCF}}$	Magnetic field strength (DCF)	$394 \pm 170 \mu\text{G}$	$417 \pm 182 \mu\text{G}$	$102 \pm 52 \mu\text{G}$
λ_{DCF}	Mass-to-flux ratio (DCF)	0.79 ± 0.34	1.12 ± 0.49	0.68 ± 0.35
$B_{\text{pos,ST}}$	Magnetic field strength (ST)	$203 \pm 87 \mu\text{G}$	$244 \pm 106 \mu\text{G}$	$70 \pm 35 \mu\text{G}$
λ_{ST}	Mass-to-flux ratio (ST)	1.54 ± 0.66	1.92 ± 0.84	1.00 ± 0.50

Table 3
Energy Distributions in the IC 348 Core Regions

Parameter	Description	HH 211 MMS	IC 348 MMS
E_G	Gravitational energy	-11 ± 14	-10 ± 12
$E_{B,\text{DCF}}$	Magnetic energy (DCF)	18 ± 16	8.8 ± 7.7
$E_{B,\text{ST}}$	Magnetic energy (ST)	4.8 ± 4.1	3.0 ± 2.6
E_{thermal}	Thermal energy	3.4 ± 2.5	2.4 ± 1.6
$E_{\text{nonthermal}}$	Turbulent energy	4.9 ± 3.5	5.2 ± 3.5

Note. Unit: 10^{42} erg.

where σ_v is a nonthermal velocity dispersion of the gas. The inferred masses and nonthermal velocity dispersions of the core regions give turbulent energies of $E_{\text{nonthermal}} = (4.9 \pm 3.5) \times 10^{42}$ erg and $(5.2 \pm 3.5) \times 10^{42}$ erg for HH 211 MMS and IC 348 MMS, respectively.

Regarding HH 211 MMS, the magnetic energy based on the DCF result dominates the energy balance. However, in the ST method gravity dominates the system, and magnetic, thermal, and turbulent energies are comparable to one another. For IC 348 MMS, the gravity and magnetic field dominate the energy balance based on the DCF result. In contrast, with the ST method, gravity dominates the system, and the turbulent energy is larger than magnetic and thermal energies.

7. Discussion

7.1. Grain Alignment in the Filament and the Two Cores

The slopes (α index) between polarization fraction and intensity reported in Section 4 and Figure 8 are shallower than 1, which suggests that there is a working alignment mechanism even in dense regions. Regarding the filament first, according to the Ricean-mean fitting that is presumably more reliable than the power-law fitting, the slope is 0.59. This could be understood with grain alignment enhanced by the radiation from the young stellar objects along the filament as shown in the positions (Figure 7) and the temperature (left panel of Figure 10; e.g., A. Lazarian & T. Hoang 2007). K. Pattle et al. (2019) suggested that a smaller α value in the Oph A region ($\alpha = 0.34$) is mainly due to the nearby two B stars of the Oph A region. A. R. Lyo et al. (2021) proposed that the lower α value for NGC 2071IR ($\alpha = 0.36$) is attributed to the additional radiation from the central three infrared young stellar objects.

In IC 348, radiations from young stellar objects along the filament could cause the shallower slope in the filament.

The slopes of the two core regions ($\alpha = 0.30$ for HH 211 MMS and $\alpha = 0.34$ for IC 348 MMS) are even smaller than that of the filament. Since the radiation from the deeply embedded protostars (HH 211 MMS and IC 348 MMS) appears weak, as indicated by the dust temperature distributions, it is uncertain whether radiation alone is responsible for the low α values in the two core regions. Grain growth in the core regions is another possibility for accounting for the lower slopes. For example, K. Pattle et al. (2021) interpreted that the inferred α value of L1689 ($\alpha \sim 0.55$) could be a sign of grain growth since a critical grain size in the region, the minimum size at which grains can be aligned by radiation, is larger than the maximum grain size in the diffuse ISM (0.25–0.3 μm ; J. S. Mathis et al. 1977). T. Hoang et al. (2021) formulated a critical grain size or alignment size (a_{align}) as follows:

$$a_{\text{align}} \simeq 0.055 \hat{\rho}^{-1/7} \left(\frac{\gamma_{-1}}{n_3 T_1} \right)^{-2/7} \left(\frac{\bar{\lambda}}{1.2 \mu\text{m}} \right)^{4/7} \times \left(\frac{T_d}{16.4 \text{ K}} \right)^{-12/7} \mu\text{m}, \quad (26)$$

where $\hat{\rho} = \rho / (3 \text{ g cm}^{-3})$ is the dust mass density, $\gamma_{-1} = \gamma / 0.1$ is the anisotropy of the radiation field, $n_3 = n_{\text{H}} / (10^3 \text{ cm}^{-3})$ is the gas density, $T_1 = T_{\text{gas}} / 10 \text{ K}$ is the gas temperature, $\bar{\lambda}$ is the mean wavelength of the stellar radiation field, and T_d is the dust temperature. We use $\gamma_{-1} = 3$ based on the finding of T. J. Bethell et al. (2007), who reported $\gamma \sim 0.3$ in molecular clouds. The mean incident wavelength in diffuse ISM is about 1.2 μm (B. T. Draine et al. 2007). According to T. Hoang et al. (2021), the mean wavelength increases in molecular clouds owing to attenuation. Therefore, we use $\bar{\lambda} = 2 \mu\text{m}$ (T. Hoang et al. 2021). Assuming $\hat{\rho} = 1$, $\gamma_{-1} = 3$, $\bar{\lambda} = 2 \mu\text{m}$, and $T_{\text{gas}} = T_{\text{dust}}$, we estimated the alignment size in IC 348 using the measured number density and dust temperature in Section 5. The distribution of alignment size in IC 348 is shown in Figure 12. The alignment size is smaller in the filament and larger in the core regions. By averaging the alignment size in the defined areas, alignment sizes for HH 211 MMS, IC 348 MMS, and the filament are estimated to be 0.39, 0.57, and 0.31 μm , respectively. Since the dust grains are well aligned in the cores, as indicated by the lower power index, a significant portion of the dust grains should be larger than the measured

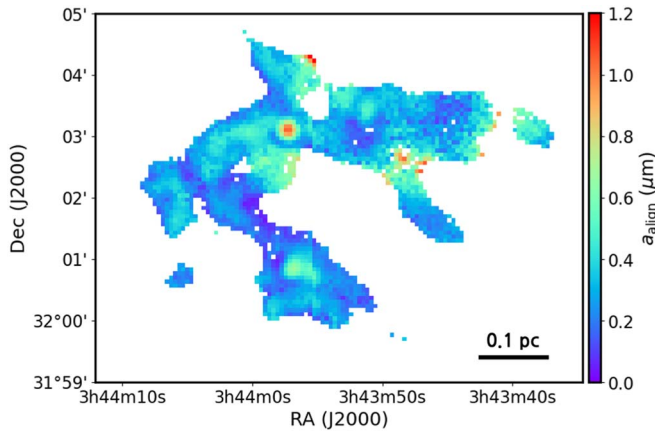


Figure 12. The estimated grain alignment size map of the IC 348 star-forming region.

alignment size. Therefore, the maximum grain sizes in the core regions are expected to be micron sizes or larger.

7.2. Transition from Magnetically Subcritical to Supercritical Condition

The measured mass-to-flux ratios are 0.45–2.20 for HH 211 MMS, 0.63–2.76 for IC 348 MMS, and 0.33–1.50 for the filament. Note that these values are upper limits, as only the plane-of-sky magnetic field components are considered. Our results suggest that the filament is likely to be subcritical, and the transition from subcritical to supercritical conditions may occur at the core scale. This is consistent with the recent picture that low-mass stars form in nearly magnetically transcritical environments (K. Pattle et al. 2023). For instance, J. Karoly et al. (2023) argued that supercritical cores form inside subcritical envelopes in L43 molecular clouds. J. Hwang et al. (2021) also found that the magnetically supercritical two clumps in the OMC-1 region are embedded in magnetically subcritical filaments. However, T. C. Ching et al. (2022a) argued that the magnetically supercritical condition is already satisfied during the formation of molecular gas clouds in the L1544 core from Zeeman measurements of HI narrow self-absorption (HINSA) lines. In this case, mass accumulation along field lines or turbulent magnetic reconnection might play more significant roles than ambipolar diffusion in reducing magnetic flux to account for an early transition (T. C. Ching et al. 2022a). The discrepancies between observations could be attributed to the geometric effects, different star-forming cloud conditions, and the uncertainties in measuring the physical quantities, such as magnetic field strengths. To evade these observation uncertainties, C. Yin et al. (2021) and F. D. Priestley et al. (2022) post-processed 3D nonideal MHD simulations and utilized a chemical network to constrain a magnetic criticality in star-forming cores. They suggested that star-forming cores form as initially magnetically subcritical conditions, consistent with the results of our study that star-forming cores form out of a subcritical parent filament. Nevertheless, further studies on the 3D structure of the magnetic field are needed to estimate accurate values of field strengths and, therefore, to constrain when and how magnetically subcritical clouds transition to supercritical star-forming cores to eventually form a star.

7.3. Stability of the Two Cores

The turbulence-to-magnetic-energy ratios are 0.25–2.00 for HH 211 MMS and 0.53–4.25 for IC 348 MMS. This result indicates that the relative strength of the turbulence to the magnetic field tends to be stronger for IC 348 MMS than for HH 211 MMS. Interferometric observations toward the two cores revealed a single source driving an outflow in HH 211 MMS, whereas three sources comprise a multiple system in IC 348 MMS (A. Palau et al. 2014; L. F. Rodríguez et al. 2014). Since turbulence promotes fragmentation when collapsing to a smaller scale and magnetic fields have the opposite effect (P. Hennebelle & S.-i. Inutsuka 2019), the energy balance at the core scale could possibly explain the different configurations inside the two cores. For HH 211 MMS strong magnetic fields lead to a single source, while for IC 348 MMS turbulence drives fragmentation, resulting in a protostellar system with multiple sources (Y.-W. Tang et al. 2019; E. J. Chung et al. 2023).

8. Conclusions

In this paper, we studied the magnetic field properties of the IC 348 star-forming region as part of the BISTRO survey. We used the 850 μm polarization data obtained with the POL-2 polarimeter on the JCMT to infer the magnetic field of the region. The magnetic field orientations in IC 348 tend to be perpendicular rather than parallel to the filamentary structure. This result supports the suggestion of P. André et al. (2014) that local magnetic fields regulate filaments in molecular clouds and is consistent with previous studies (e.g., D. Ward-Thompson et al. 2017; W. Kwon et al. 2022).

We measured the power-law index of the relation between the polarization fraction and total intensity using two independent methods: the power law and the mean of the Rice distribution methods. We found that the inferred power indices are larger for the power-law method than for the Ricean-mean method, as expected by K. Pattle et al. (2019). The Ricean-mean method provides power-law indices of 0.59, 0.30, and 0.34 for the filament, HH 211 MMS, and IC 348 MMS, respectively. This result indicates that dust grains are well aligned even in high-density regions, justifying the use of polarization observations to infer the region’s magnetic field. Relatively low power-law index values in the protostellar cores could be attributed to grain growth to micron size or larger in the cores.

The magnetic field strengths of HH 211 MMS, IC 348 MMS, and the filament were measured using the DCF method and the ST modification suggested by R. Skalidis & K. Tassis (2021). The measured mass-to-flux ratios are 0.45–2.20 and 0.63–2.76 for HH 211 MMS and IC 348 MMS, respectively, while the ratios for the filament are 0.33–1.50. These results are upper limits, as only the plane-of-sky magnetic fields are considered. Thus, our results suggest that the filament is likely to be magnetically subcritical, where the magnetic field may support the gravitational collapse on the filament scale (~ 0.5 pc). The transition from subcritical to supercritical conditions may occur at the core scale (~ 0.05 pc).

Lastly, we studied the energy balances of the two core regions. We measured the gravitational, magnetic, thermal, and turbulent energies of the two cores. The turbulence with respect to the magnetic field is likely to be stronger in IC 348 MMS than in HH 211 MMS, which could possibly explain the different configurations inside the two cores: a single protostellar system in HH 211 MMS and multiple protostellar systems in IC 348 MMS.

Acknowledgments

We are grateful to the anonymous referee for helpful comments. This work was supported by the National Research Foundation of Korea (NRF) grants funded by the Korea government (MSIT) (RS-2024-00342488 and RS-2024-00416859). K.P. is a Royal Society University Research Fellow, supported by grant No. URF\R1\211322. F.P. acknowledges support from the Spanish MICINN under grant No. PID2022-141915NB-C21. S.-P.L. and M.-Z.Y. acknowledge the support of the National Science and Technology Council of Taiwan under project Nos. 112-2112-M-007-011 and 113-2112-M-007-004. K.Q. acknowledges supports from National Natural Science Foundation of China (NSFC) grants 12425304 and U1731237, and National Key R&D Program of China No. 2023YFA1608204 and No. 2022YFA1603100. L.F. acknowledges support from the Ministry of Science and Technology of Taiwan under grant No. 111-2112-M-005-018-MY3. D.J. is supported by NRC Canada and by an NSERC Discovery Grant. M.R. is supported by the international Gemini Observatory, a program of NSF NOIRLab, which is managed by the Association of Universities for Research in Astronomy (AURA) under a cooperative agreement with the U.S. National Science Foundation, on behalf of the Gemini partnership of Argentina, Brazil, Canada, Chile, the Republic of Korea, and the United States of America.




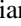

The James Clerk Maxwell Telescope (JCMT) is operated by the East Asian Observatory on behalf of The National Astronomical Observatory of Japan, Academia Sinica Institute of Astronomy and Astrophysics, the Korea Astronomy and Space Science Institute, the National Astronomical Research Institute of Thailand, and the Center for Astronomical Mega-Science (as well as the National Key R&D Program of China with No. 2017YFA0402700). Additional funding support is provided by the Science and Technology Facilities Council of the United Kingdom and participating universities and organizations in the United Kingdom, Canada, and Ireland. Additional funds for the construction of SCUBA-2 and POL-2 were provided by the Canada Foundation for Innovation. The JCMT has historically been operated by the Joint Astronomy Centre on behalf of the Science and Technology Facilities Council of the United Kingdom, the National Research Council of Canada, and the Netherlands Organisation for Scientific Research. The POL-2 data used in this paper were taken under project code M17BL011, and the HARP data were taken under project code M06BGT02.

The authors wish to recognize and acknowledge the very significant cultural role and reverence that the summit of Maunakea has always had within the indigenous Hawaiian community. We are most fortunate to have the opportunity to conduct observations from this mountain.



Facility: JCMT.

Software: Starlink (M. J. Currie et al. 2014), SMURF (E. L. Chapin et al. 2013).

ORCID iDs

Youngwoo Choi  <https://orcid.org/0009-0004-9279-780X>
 Woojin Kwon  <https://orcid.org/0000-0003-4022-4132>
 Kate Pattle  <https://orcid.org/0000-0002-8557-3582>
 Doris Arzoumanian  <https://orcid.org/0000-0002-1959-7201>
 Tyler L. Bourke  <https://orcid.org/0000-0001-7491-0048>

Thiem Hoang  <https://orcid.org/0000-0003-2017-0982>
 Jihye Hwang  <https://orcid.org/0000-0001-7866-2686>
 Patrick M. Koch  <https://orcid.org/0000-0003-2777-5861>
 Pierre Bastien  <https://orcid.org/0000-0002-0794-3859>
 Shih-Ping Lai  <https://orcid.org/0000-0001-5522-486X>
 Keping Qiu  <https://orcid.org/0000-0002-5093-5088>
 Derek Ward-Thompson  <https://orcid.org/0000-0003-1140-2761>
 David Berry  <https://orcid.org/0000-0001-6524-2447>
 Huei-Ru Vivien Chen  <https://orcid.org/0000-0002-9774-1846>
 Wen Ping Chen  <https://orcid.org/0000-0003-0262-272X>
 Tao-Chung Ching  <https://orcid.org/0000-0001-8516-2532>
 Simon Coudé  <https://orcid.org/0000-0002-0859-0805>
 Eun Jung Chung  <https://orcid.org/0000-0003-0014-1527>
 Victor Debattista  <https://orcid.org/0000-0001-7902-0116>
 James Di Francesco  <https://orcid.org/0000-0002-9289-2450>
 Pham Ngoc Diep  <https://orcid.org/0000-0002-2808-0888>
 Yasuo Doi  <https://orcid.org/0000-0001-8746-6548>
 Chakali Eswarajah  <https://orcid.org/0000-0003-4761-6139>
 Lapo Fanciullo  <https://orcid.org/0000-0001-9930-9240>
 Laura M. Fissel  <https://orcid.org/0000-0002-4666-609X>
 Tim Gledhill  <https://orcid.org/0000-0002-2859-4600>
 Tetsuo Hasegawa  <https://orcid.org/0000-0003-1853-0184>
 Charles L. H. Hull  <https://orcid.org/0000-0002-8975-7573>
 Tsuyoshi Inoue  <https://orcid.org/0000-0002-7935-8771>
 Shu-ichiro Inutsuka  <https://orcid.org/0000-0003-4366-6518>
 Il-Gyo Jeong  <https://orcid.org/0000-0002-5492-6832>
 Doug Johnstone  <https://orcid.org/0000-0002-6773-459X>
 Janik Karoly  <https://orcid.org/0000-0001-5996-3600>
 Ji-hyun Kang  <https://orcid.org/0000-0001-7379-6263>
 Miju Kang  <https://orcid.org/0000-0002-5016-050X>
 Francisca Kemper  <https://orcid.org/0000-0003-2743-8240>
 Jongsoo Kim  <https://orcid.org/0000-0002-1229-0426>
 Shinyoung Kim  <https://orcid.org/0000-0001-9333-5608>
 Gwanjeong Kim  <https://orcid.org/0000-0003-2011-8172>
 Kyoung Hee Kim  <https://orcid.org/0000-0001-9597-7196>
 Kee-Tae Kim  <https://orcid.org/0000-0003-2412-7092>
 Florian Kirchschrager  <https://orcid.org/0000-0002-3036-0184>
 Jason Kirk  <https://orcid.org/0000-0002-4552-7477>
 Masato I. N. Kobayashi  <https://orcid.org/0000-0003-3990-1204>
 Jungmi Kwon  <https://orcid.org/0000-0003-2815-7774>
 Chang Won Lee  <https://orcid.org/0000-0002-3179-6334>
 Sheng-Jun Lin  <https://orcid.org/0000-0002-6868-4483>
 Hong-Li Liu  <https://orcid.org/0000-0003-3343-9645>
 Tie Liu  <https://orcid.org/0000-0002-5286-2564>
 Sheng-Yuan Liu  <https://orcid.org/0000-0003-4603-7119>
 Junhao Liu  <https://orcid.org/0000-0002-4774-2998>
 Steven Longmore  <https://orcid.org/0000-0001-6353-0170>
 Xing Lu  <https://orcid.org/0000-0003-2619-9305>
 Steve Mairs  <https://orcid.org/0000-0002-6956-0730>
 Masafumi Matsumura  <https://orcid.org/0000-0002-6906-0103>
 Gerald Moriarty-Schieven  <https://orcid.org/0000-0002-0393-7822>
 Nguyen Bich Ngoc  <https://orcid.org/0000-0002-5913-5554>
 Nagayoshi Ohashi  <https://orcid.org/0000-0003-0998-5064>
 Takashi Onaka  <https://orcid.org/0000-0002-8234-6747>
 Jonathan Rawlings  <https://orcid.org/0000-0001-5560-1303>
 Mark Rawlings  <https://orcid.org/0000-0002-6529-202X>
 Ekta Sharma  <https://orcid.org/0000-0002-4541-0607>
 Yoshito Shimajiri  <https://orcid.org/0000-0001-9368-3143>
 Archana Soam  <https://orcid.org/0000-0002-6386-2906>
 Mehrnoosh Tahani  <https://orcid.org/0000-0001-8749-1436>

Motohide Tamura  <https://orcid.org/0000-0002-6510-0681>
 Xindi Tang  <https://orcid.org/0000-0002-4154-4309>
 Kohji Tomisaka  <https://orcid.org/0000-0003-2726-0892>
 Le Ngoc Tram  <https://orcid.org/0000-0002-6488-8227>
 Jia-Wei Wang  <https://orcid.org/0000-0002-6668-974X>
 Anthony Whitworth  <https://orcid.org/0000-0002-1178-5486>
 Jinjin Xie  <https://orcid.org/0000-0002-2738-146X>
 Meng-Zhe Yang  <https://orcid.org/0009-0003-5699-2723>
 Hyunju Yoo  <https://orcid.org/0000-0002-8578-1728>
 Hyeong-Sik Yun  <https://orcid.org/0000-0001-6842-1555>
 Yapeng Zhang  <https://orcid.org/0000-0002-5102-2096>
 Jianjun Zhou  <https://orcid.org/0000-0003-0356-818X>
 David Eden  <https://orcid.org/0000-0002-5881-3229>
 Sam Falle  <https://orcid.org/0000-0002-9829-0426>
 Valentin J. M. Le Gouellec  <https://orcid.org/0000-0002-5714-799X>
 Frédérick Poidevin  <https://orcid.org/0000-0002-5391-5568>

References

- Alina, D., Ristorcelli, I., Montier, L., et al. 2019, *MNRAS*, **485**, 2825
 Andersson, B. G., Lazarian, A., & Vaillancourt, J. E. 2015, *ARA&A*, **53**, 501
 André, P., Di Francesco, J., Ward-Thompson, D., et al. 2014, in *Protostars and Planets VI*, ed. H. Beuther et al. (Tucson, AZ: Univ. of Arizona Press), 27
 André, P., Men'shchikov, A., Bontemps, S., et al. 2010, *A&A*, **518**, L102
 Arzoumanian, D., André, P., Didelon, P., et al. 2011, *A&A*, **529**, L6
 Arzoumanian, D., Furuya, R. S., Hasegawa, T., et al. 2021, *A&A*, **647**, A78
 Bally, J., Walawender, J., Johnstone, D., Kirk, H., & Goodman, A. 2008, in *Handbook of Star Forming Regions, Volume I*, ed. B. Reipurth, 4 (San Francisco, CA: ASP), 308
 Barnes, A. T., Longmore, S. N., Battersby, C., et al. 2017, *MNRAS*, **469**, 2263
 Beckwith, S. V. W., & Sargent, A. I. 1991, *ApJ*, **381**, 250
 Bell, C. P. M., Naylor, T., Mayne, N. J., Jeffries, R. D., & Littlefair, S. P. 2013, *MNRAS*, **434**, 806
 Bethell, T. J., Chepurinov, A., Lazarian, A., & Kim, J. 2007, *ApJ*, **663**, 1055
 Buckle, J. V., Hills, R. E., Smith, H., et al. 2009, *MNRAS*, **399**, 1026
 Carpenter, J. M. 2000, *AJ*, **120**, 3139
 Chandrasekhar, S., & Fermi, E. 1953, *ApJ*, **118**, 113
 Chapin, E. L., Berry, D. S., Gibb, A. G., et al. 2013, *MNRAS*, **430**, 2545
 Ching, T. C., Li, D., Heiles, C., et al. 2022a, *Natur*, **601**, 49
 Ching, T.-C., Qiu, K., Li, D., et al. 2022b, *ApJ*, **941**, 122
 Cho, J., & Yoo, H. 2016, *ApJ*, **821**, 21
 Chung, E. J., Lee, C. W., Kwon, W., et al. 2023, *ApJ*, **951**, 68
 Coudé, S., Bastien, P., Houde, M., et al. 2019, *ApJ*, **877**, 88
 Cox, N. L. J., Arzoumanian, D., André, P., et al. 2016, *A&A*, **590**, A110
 Crutcher, R. M., Nutter, D. J., Ward-Thompson, D., & Kirk, J. M. 2004, *ApJ*, **600**, 279
 Currie, M. J., Berry, D. S., Jenness, T., et al. 2014, in *ASP Conf. Ser. 485, Astronomical Data Analysis Software and Systems XXIII*, ed. N. Manset & P. Forshay (San Francisco, CA: ASP), 391
 Curtis, E. I., Richer, J. S., & Buckle, J. V. 2010, *MNRAS*, **401**, 455
 Davis, L. 1951, *PhRv*, **81**, 890
 Davis, L. J., & Greenstein, J. L. 1951, *ApJ*, **114**, 206
 Dempsey, J. T., Friberg, P., Jenness, T., et al. 2013, *MNRAS*, **430**, 2534
 Doi, Y., Hasegawa, T., Furuya, R. S., et al. 2020, *ApJ*, **899**, 28
 Doi, Y., Tomisaka, K., Hasegawa, T., et al. 2021, *ApJL*, **923**, L9
 Draine, B. T., Dale, D. A., Bendo, G., et al. 2007, *ApJ*, **663**, 866
 Draine, B. T., & Weingartner, J. C. 1997, *ApJ*, **480**, 633
 Eisloffel, J., Froebrich, D., Stanke, T., & McCaughrean, M. J. 2003, *ApJ*, **595**, 259
 Evans, N. J. I., Dunham, M. M., Jørgensen, J. K., et al. 2009, *ApJS*, **181**, 321
 Fernández-López, M., Arce, H. G., Looney, L., et al. 2014, *ApJL*, **790**, L19
 Fissel, L. M., Ade, P. A. R., Angilè, F. E., et al. 2019, *ApJ*, **878**, 110
 Friberg, P., Bastien, P., Berry, D., et al. 2016, *Proc. SPIE*, **9914**, 991403
 Gould, B. A. 1879, *RNAO*, **1**, I
 Hacar, A., Tafalla, M., Kauffmann, J., & Kovács, A. 2013, *A&A*, **554**, A55
 Hennebelle, P., & Inutsuka, S.-i. 2019, *FrASS*, **6**, 5
 Herbst, W. 2008, in *Handbook of Star Forming Regions, Volume I*, ed. B. Reipurth, Vol. 4 (San Francisco, CA: ASP), 372
 Herschel, J. F. W. S. 1847, *Results of Astronomical Observations made during the years 1834, 5, 6, 7, 8, at the Cape of Good Hope; being the Completion of a Telescopic Survey of the Whole Surface of the Visible Heavens, Commenced in 1825* (London: Smith, Elder, Co.)
 Hildebrand, R. H. 1983, *QJRAS*, **24**, 267
 Hildebrand, R. H., Kirby, L., Dotson, J. L., Houde, M., & Vaillancourt, J. E. 2009, *ApJ*, **696**, 567
 Hoang, T., & Lazarian, A. 2016, *ApJ*, **831**, 159
 Hoang, T., Tram, L. N., Lee, H., Diep, P. N., & Ngoc, N. B. 2021, *ApJ*, **908**, 218
 Holland, W. S., Bintley, D., Chapin, E. L., et al. 2013, *MNRAS*, **430**, 2513
 Houde, M., Vaillancourt, J. E., Hildebrand, R. H., Chitsazzadeh, S., & Kirby, L. 2009, *ApJ*, **706**, 1504
 Hull, C. L. H., & Zhang, Q. 2019, *FrASS*, **6**, 3
 Hwang, J., Kim, J., Pattle, K., et al. 2021, *ApJ*, **913**, 85
 Hwang, J., Kim, J., Pattle, K., et al. 2022, *ApJ*, **941**, 51
 Jones, T. J., Bagley, M., Krejny, M., Andersson, B. G., & Bastien, P. 2015, *AJ*, **149**, 31
 Karoly, J., Ward-Thompson, D., Pattle, K., et al. 2023, *ApJ*, **952**, 29
 Kirk, H., Johnstone, D., & Tafalla, M. 2007, *ApJ*, **668**, 1042
 Kirk, J. M., Ward-Thompson, D., Palmeirim, P., et al. 2013, *MNRAS*, **432**, 1424
 Koch, E. W., & Rosolowsky, E. W. 2015, *MNRAS*, **452**, 3435
 Kwon, W., Looney, L. W., Mundy, L. G., Chiang, H.-F., & Kemball, A. J. 2009, *ApJ*, **696**, 841
 Kwon, W., Pattle, K., Sadavoy, S., et al. 2022, *ApJ*, **926**, 163
 Lazarian, A., & Hoang, T. 2007, *MNRAS*, **378**, 910
 Lazarian, A., Yuen, K. H., & Pogosyan, D. 2022, *ApJ*, **935**, 77
 Li, P. S., Lopez-Rodriguez, E., Ajeddig, H., et al. 2022, *MNRAS*, **510**, 6085
 Lin, Y., Liu, H. B., Li, D., et al. 2016, *ApJ*, **828**, 32
 Liu, J., Qiu, K., Berry, D., et al. 2019, *ApJ*, **877**, 43
 Liu, J., Zhang, Q., Commerçon, B., et al. 2021, *ApJ*, **919**, 79
 Liu, J., Zhang, Q., & Qiu, K. 2022, *FrASS*, **9**, 943556
 Liu, T., Li, P. S., Juvela, M., et al. 2018, *ApJ*, **859**, 151
 Luhman, K. L., Esplin, T. L., & Loutrel, N. P. 2016, *ApJ*, **827**, 52
 Luhman, K. L., Stauffer, J. R., Muench, A. A., et al. 2003, *ApJ*, **593**, 1093
 Lyo, A. R., Kim, J., Sadavoy, S., et al. 2021, *ApJ*, **918**, 85
 Mairs, S., Dempsey, J. T., Bell, G. S., et al. 2021, *AJ*, **162**, 191
 Mathis, J. S., Rumpl, W., & Nordsieck, K. H. 1977, *ApJ*, **217**, 425
 Matthews, B. C., McPhee, C. A., Fissel, L. M., & Curran, R. L. 2009, *ApJS*, **182**, 143
 McCaughrean, M. J., Rayner, J. T., & Zinnecker, H. 1994, *ApJL*, **436**, L189
 Nakano, T., & Nakamura, T. 1978, *PASJ*, **30**, 671
 Ortiz-León, G. N., Loinard, L., Dzib, S. A., et al. 2018, *ApJ*, **865**, 73
 Ostriker, E. C., Stone, J. M., & Gammie, C. F. 2001, *ApJ*, **546**, 980
 Padoan, P., Federrath, C., Chabrier, G., et al. 2014, in *Protostars and Planets VI*, ed. H. Beuther et al. (Tucson, AZ: Univ. of Arizona Press), 77
 Padoan, P., Goodman, A., Draine, B. T., et al. 2001, *ApJ*, **559**, 1005
 Palau, A., Zapata, L. A., Rodríguez, L. F., et al. 2014, *MNRAS*, **444**, 833
 Palmeirim, P., André, P., Kirk, J., et al. 2013, *A&A*, **550**, A38
 Pattle, K., Fissel, L., Tahani, M., Liu, T., & Ntormousi, E. 2023, in *ASP Conf. Ser. 534, Protostars and Planets VII*, ed. S. Inutsuka et al. (San Francisco, CA: ASP), 193
 Pattle, K., Lai, S.-P., Di Francesco, J., et al. 2021, *ApJ*, **907**, 88
 Pattle, K., Lai, S.-P., Hasegawa, T., et al. 2019, *ApJ*, **880**, 27
 Pattle, K., Ward-Thompson, D., Berry, D., et al. 2017a, *ApJ*, **846**, 122
 Pattle, K., Ward-Thompson, D., Kirk, J. M., et al. 2017b, *MNRAS*, **464**, 4255
 Pillai, T. G. S., Clemens, D. P., Reissl, S., et al. 2020, *NatAs*, **4**, 1195
 Planck Collaboration, Adam, R., Ade, P. A. R., et al. 2016, *A&A*, **586**, A135
 Pokhrel, R., Myers, P. C., Dunham, M. M., et al. 2018, *ApJ*, **853**, 5
 Priestley, F. D., Yin, C., & Wurster, J. 2022, *MNRAS*, **515**, 5689
 Purcell, E. M. 1979, *ApJ*, **231**, 404
 Rodríguez, L. F., Zapata, L. A., & Palau, A. 2014, *ApJ*, **790**, 80
 Roy, A., André, P., Palmeirim, P., et al. 2014, *A&A*, **562**, A138
 Sadavoy, S. I., Di Francesco, J., Johnstone, D., et al. 2013, *ApJ*, **767**, 126
 Sadavoy, S. I., Stutz, A. M., Schnee, S., et al. 2016, *A&A*, **588**, A30
 Schisano, E., Rygl, K. L. J., Molinari, S., et al. 2014, *ApJ*, **791**, 27
 Skalidis, R., & Tassis, K. 2021, *A&A*, **647**, A186
 Soam, A., Liu, T., Andersson, B. G., et al. 2019, *ApJ*, **883**, 95
 Soler, J. D., Hennebelle, P., Martin, P. G., et al. 2013, *ApJ*, **774**, 128
 Stephens, I. W., Dunham, M. M., Myers, P. C., et al. 2017, *ApJ*, **846**, 16
 Strom, S. E., Strom, K. M., & Carrasco, L. 1974, *PASP*, **86**, 798
 Tahani, M. 2022, *FrASS*, **9**, 940027
 Tahani, M., Bastien, P., Furuya, R. S., et al. 2023, *ApJ*, **944**, 139
 Tahani, M., Lupypciw, W., Glover, J., et al. 2022, *A&A*, **660**, A97
 Tang, Y.-W., Koch, P. M., Peretto, N., et al. 2019, *ApJ*, **878**, 10
 Tobin, J. J., Looney, L. W., Li, Z.-Y., et al. 2016, *ApJ*, **818**, 73

- Walawender, J., Bally, J., Francesco, J. D., Jørgensen, J., & Getman, K. 2008, in *Handbook of Star Forming Regions, Volume I*, ed. B. Reipurth, 4 (San Francisco, CA: ASP), [346](#)
- Wang, J.-W., Lai, S.-P., Eswarajah, C., et al. 2019, [ApJ](#), **876**, 42
- Wardle, J. F. C., & Kronberg, P. P. 1974, [ApJ](#), **194**, 249
- Ward-Thompson, D., Di Francesco, J., Hatchell, J., et al. 2007, [PASP](#), **119**, 855
- Ward-Thompson, D., Karoly, J., Pattle, K., et al. 2023, [ApJ](#), **946**, 62
- Ward-Thompson, D., Pattle, K., Bastien, P., et al. 2017, [ApJ](#), **842**, 66
- Whittet, D. C. B., Hough, J. H., Lazarian, A., & Hoang, T. 2008, [ApJ](#), **674**, 304
- Yen, H.-W., Koch, P. M., Hull, C. L. H., et al. 2021, [ApJ](#), **907**, 33
- Yin, C., Priestley, F. D., & Wurster, J. 2021, [MNRAS](#), **504**, 2381
- Zucker, C., Schlafly, E. F., Speagle, J. S., et al. 2018, [ApJ](#), **869**, 83